NAVAL POSTGRADUATE SCHOOL

MONTEREY, CALIFORNIA

THESIS

INFLUENCE OF THE AS-PRINTING AND POST-PRINTING PROCESSES ON THE MECHANICAL PROPERTIES OF LIQUID METAL JETTED 3D PARTS

by

Kahra L. Kelty

June 2022

Thesis Advisor: Claudia C. Luhrs
Co-Advisor: David F. Dausen

THIS PAGE INTENTIONALLY LEFT BLANK

REPORT DOCUMENTATION PAGE	*Form Approved OMB No. 0704-0188*

1. AGENCY USE ONLY ***(Leave blank)***	**2. REPORT DATE** June 2022	**3. REPORT TYPE AND DATES COVERED** Master's thesis

4. TITLE AND SUBTITLE
INFLUENCE OF THE AS-PRINTING AND POST-PRINTING PROCESSES ON THE MECHANICAL PROPERTIES OF LIQUID METAL JETTED 3D PARTS

5. FUNDING NUMBERS

6. AUTHOR(S) Kahra L. Kelty

7. PERFORMING ORGANIZATION NAME(S) AND ADDRESS(ES)
Naval Postgraduate School
Monterey, CA 93943-5000

8. PERFORMING ORGANIZATION REPORT NUMBER

9. SPONSORING / MONITORING AGENCY NAME(S) AND ADDRESS(ES)
N/A

10. SPONSORING / MONITORING AGENCY REPORT NUMBER

11. SUPPLEMENTARY NOTES The views expressed in this thesis are those of the author and do not reflect the official policy or position of the Department of Defense or the U.S. Government.

12a. DISTRIBUTION / AVAILABILITY STATEMENT
Approved for public release. Distribution is unlimited.

12b. DISTRIBUTION CODE
A

13. ABSTRACT (maximum 200 words)

Heat treatable aluminum alloys require post-fabrication steps to achieve the desired properties. The conditions to treat cast aluminum parts are well established, however the same processes are not well studied for additive manufactured (AM) parts. This study evaluated the effects of post-printing processes on the hardness of metal parts fabricated by AM. The research focused on the intermediate period from print completion to immersion of the sample into the quenching bath and how delays can influence the part's hardness. Those results were compared to samples that were then solution treated. Aging procedures were conducted to evaluate the influence of diverse time and temperature on hardness. In addition to post-printing process studies, an experiment was conducted to evaluate the effects of introducing additional argon into the printing environment as the 3D part is produced. It was found that quenching after the initial minute of print completion has lasting effects on hardness that are not reversed by the solution treatment step at the temperatures and times employed. Modifying the standard aging time and temperature by ± 15ºC or ± 20 minutes did not show a significant effect on the mechanical properties of the prints (<3% change in hardness). Samples that were heat treated increased in hardness, demonstrating the usefulness of the T6 heat treatment. The 3D printer was employed to fabricate the component used to distribute extra argon into the printing environment.

14. SUBJECT TERMS
3D printing, solution treatment, quenching, Vickers Hardness, grain boundaries, tensile testing, 4008, A356, Xerox, ElemX, additive manufacturing, material jetting, liquid metal jetting

15. NUMBER OF PAGES
89

16. PRICE CODE

17. SECURITY CLASSIFICATION OF REPORT	**18. SECURITY CLASSIFICATION OF THIS PAGE**	**19. SECURITY CLASSIFICATION OF ABSTRACT**	**20. LIMITATION OF ABSTRACT**
Unclassified	Unclassified	Unclassified	UU

NSN 7540-01-280-5500

Standard Form 298 (Rev. 2-89)
Prescribed by ANSI Std. 239-18

THIS PAGE INTENTIONALLY LEFT BLANK

Approved for public release. Distribution is unlimited.

INFLUENCE OF THE AS-PRINTING AND POST-PRINTING PROCESSES ON THE MECHANICAL PROPERTIES OF LIQUID METAL JETTED 3D PARTS

Kahra L. Kelty
Lieutenant, United States Navy
BS, United States Naval Academy, 2015

Submitted in partial fulfillment of the
requirements for the degree of

MASTER OF SCIENCE IN MECHANICAL ENGINEERING

from the

NAVAL POSTGRADUATE SCHOOL
June 2022

Approved by: Claudia C. Luhrs
Advisor

David F. Dausen
Co-Advisor

Garth V. Hobson
Chair, Department of Mechanical and Aerospace Engineering

THIS PAGE INTENTIONALLY LEFT BLANK

ABSTRACT

Heat treatable aluminum alloys require post-fabrication steps to achieve the desired properties. The conditions to treat cast aluminum parts are well established, however the same processes are not well studied for additive manufactured (AM) parts. This study evaluated the effects of post-printing processes on the hardness of metal parts fabricated by AM. The research focused on the intermediate period from print completion to immersion of the sample into the quenching bath and how delays can influence the part's hardness. Those results were compared to samples that were then solution treated. Aging procedures were conducted to evaluate the influence of diverse time and temperature on hardness. In addition to post-printing process studies, an experiment was conducted to evaluate the effects of introducing additional argon into the printing environment as the 3D part is produced. It was found that quenching after the initial minute of print completion has lasting effects on hardness that are not reversed by the solution treatment step at the temperatures and times employed. Modifying the standard aging time and temperature by ± 15ºC or ± 20 minutes did not show a significant effect on the mechanical properties of the prints (<3% change in hardness). Samples that were heat treated increased in hardness, demonstrating the usefulness of the T6 heat treatment. The 3D printer was employed to fabricate the component used to distribute extra argon into the printing environment.

THIS PAGE INTENTIONALLY LEFT BLANK

TABLE OF CONTENTS

LIST OF FIGURES

LIST OF TABLES

THIS PAGE INTENTIONALLY LEFT BLANK

LIST OF ACRONYMS AND ABBREVIATIONS

AM	Additive Manufacturing
ASTM	American Society for Testing and Materials
BJT	Binder Jetting
CAD	Computer-Aided Design
DED	Directed Energy Deposition
EDS	Energy Dispersive X-ray Spectroscopy
EOS	Electro Optical Systems
HV	Vickers Hardness Value
ISO	International Organization for Standardization
LMJ	Liquid Metal Jet
MEX	Material Extrusion
Mg_2Si	Magnesium Silicide
MJT	Material Jetting
OM	Optical Microscopy
PBF	Powder Bed Fusion
SEM	Scanning Electron Microscopy
SHL	Sheet Lamination
Si	Silicon
UTS	Ultimate Tensile Strength
VPP	Vat Photopolymerization
YS	Yield Tensile Strength

THIS PAGE INTENTIONALLY LEFT BLANK

ACKNOWLEDGMENTS

I want to take this opportunity to thank my advisor, Claudia Luhrs, for the mentorship you provided throughout my time at NPS. Also, thank you to my co-advisor, David Dausen, for the constant support throughout the thesis process. I especially want to thank my mother, Frank Kelty, for showing me what it takes to be a strong woman. You always believed in me. You have always shown me grace and kindness when I needed it the most. Thank you for your patience and inspiration.

THIS PAGE INTENTIONALLY LEFT BLANK

I. INTRODUCTION

Additive manufacturing (AM) allows parts to be printed and ready for install in as little as hours compared to the current supply chain that can take up to weeks, if not months, to deliver the same part. The 2018 National Defense Strategy (NDS) identifies additive manufacturing as a key strategy to improve logistical and operational processes with its added benefit of "speed and flexibility" [1]. AM involves several steps to produce a final part. The specimen, first, must be designed and then printed. After printing, the part is quenched and heat treated. Heat treatments greatly improve the mechanical properties of the part by influencing the microstructural features. For this study, the T6 heat treatment was evaluated for applicability on additively manufactured parts focusing on material jetted 3D parts.

The seven categories of additive manufacturing identified by the International Organization for Standardization/American Society for Testing and Materials (ISO/ASTM) are binder jetting (BJT), directed energy deposition (DED), material extrusion (MEX), material jetting (MJT), powder bed fusion (PBF), sheet lamination (SHL), and vat photopolymerization (VPP) [2]. Depending on the process, the material can be a variety of ceramics, polymers, and metals in either powder or wire form. Figure 1 depicts all seven AM processes.

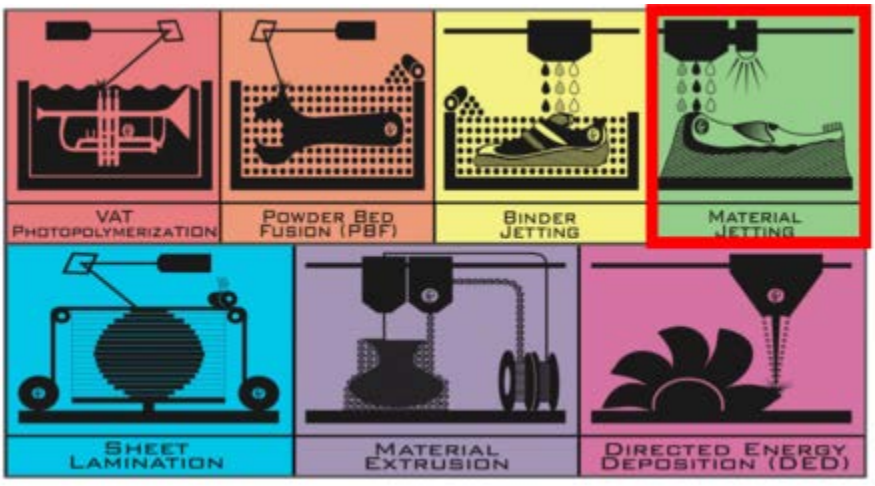

Figure 1. The Seven ISO/ASTM Recognized Additive Manufacturing Processes. Adapted from [3]

The Xerox ElemX liquid metal printer, used in this study, falls under MJT as a subgroup producing its prints via liquid metal jetting (LMJ). MJT defined by ISO/ASTM standard is a “process in which droplets of feedstock material are selectively deposited” [2]. The ElemX printer uses wire-fed metal instead of powder metal. That brings a great advantage because it eliminates the safety concerns related with storing powder metal due to its pyrophoric properties [4].

The Xerox ElemX liquid metal printer that was used to conduct the experiments and is shown in Figure 2. The liquid metal printer weighs 2,145.5 kg (4,730 lbs.) and measures 6.25 meters x 3.78 meters x 3.14 meters (20.5 feet x 12.4 feet x 10.3 feet) [5]. The size and weight are reasonable for use on a ship or as a deployable entity. For the experiments, the parts were printed using Al 4008 alloy and can be compared to A356 cast alloy.

The studies presented in this thesis sought to answer if the initial quenching conditions, employed right after the part 3D printing operation is completed, had lasting effects on the 3D parts mechanical properties and if they are reversible with the solution treatment time and temperature applied. Following, this research determined if the aging time and temperatures used for A356 cast aluminum can also be applied to additive manufactured parts. For these studies, the samples’ hardness and silicon and magnesium silicide particle sizes were measured to be compared. Finally, this research explored different printing conditions that will ultimately improve the 3D parts quality by investigating if added argon to the printing environment can overcome the present issues such as oxidation and gas porosity.

Figure 2. Xerox ElemX Liquid Metal Printer with Build Plate Transfer Crane. Source: [6]

A. LIQUID METAL JETTING (LMJ)

LMJ functions in the same way as an inkjet [7]. Al 4008 wire is fed from a spool into the printhead region of the 3D printer where it is heated in a chamber to molten form. From there, the molten material is forced into a nozzle by a "pulse of pressure" generated in the chamber [7]. As the column of molten material in the nozzle builds up, a surface tension is created that then causes spherical droplets to form as it leaves the nozzle. The consistency for the release of the droplets is controlled by "pulsed magnetic and electrical induction through the molten aluminum [that] produces a Lorentz force" [7]. Figure 3, Figure 4 and Figure 5 diagrams how the wire-fed Al 4008 is fed into the printhead region, melted into molten material, and then deposited from the nozzle as spherical droplets.

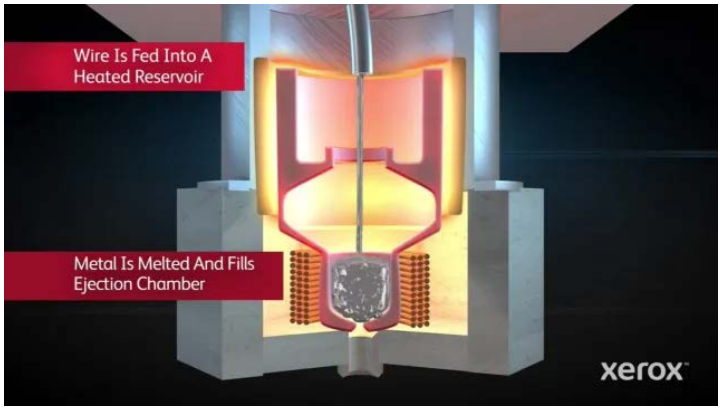

Figure 3. Printhead Region Depicting Wire-fed Material Melted and Fed to Nozzle. Source: [8]

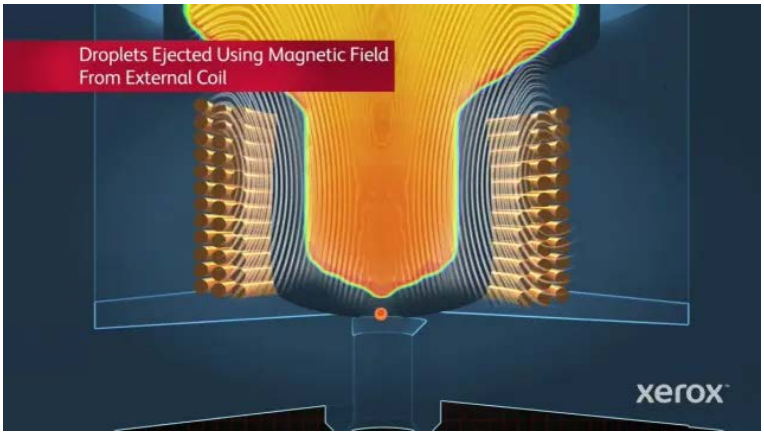

Figure 4. Droplet of Al 4008 From Nozzle. Source: [8]

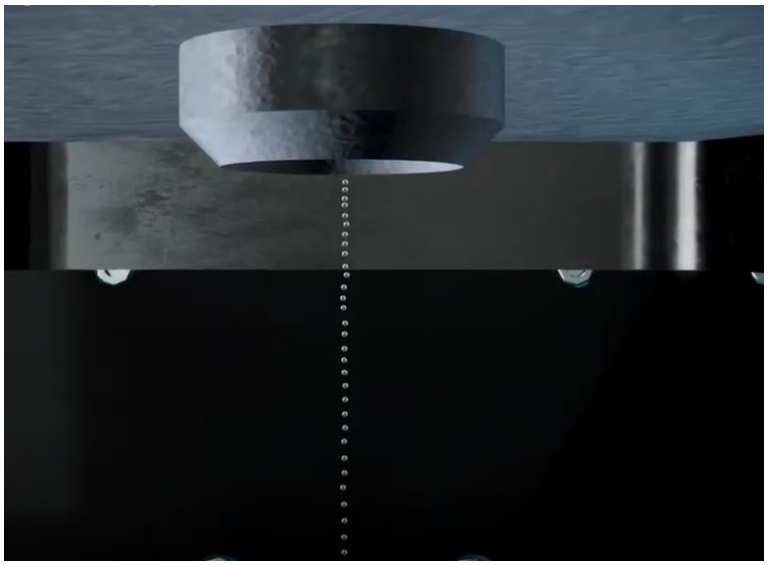

Figure 5. Depiction of Al 4008 Molten Droplets Leaving Nozzle. Source: [6]

The Xerox ElemX liquid metal printer's jetted liquid droplets form in layers either in a horizontal or vertical print pattern. Each print direction is identified as either XY or Z orientation respectively.

B. AL 4008/A356 METALLOGRAPHY

The ElemX metal liquid 3D printer uses wire-fed aluminum 4008 wrought alloy, or Al 4008, and is comparable to A356 cast alloy. The composition, by wt%, of Al 4008 compared to A356 is provided in Table 1 with the remainder being aluminum.

Table 1. Al 4008 Composition by wt%. Adapted From [9], [10]

Aluminum Association	**Si**	**Mg**	**Ti**	**Fe**	**Cu**	**Zn**	**Mn**
Al 4008	6.5-7.5	0.30-0.45	0.04-0.15	0.08	0.05	0.05	0.05
A356	6.5-7.5	0.25-0.45	0.20	0.20	0.20	0.10	0.10

The Aluminum Association is widely used in the United States and identifies the 4xxx wrought group as the Al-Si alloy family where silicon is its principal alloying element [11]. Of the Al alloys, Al-Si alloys are the most commonly used in AM [12]. The addition of magnesium to the Al-Si alloy allows it to be age hardenable [13].

The difference between wrought and cast is the way the metal is manufactured. Cast alloys are melted in a "furnace and poured into a mold" while wrought is "worked in the solid form with the help of specific tools" to make into the desired shape. Wrought alloys are more expensive compared to cast alloys but have improved mechanical properties. The Al 4008's density at 2.66 gm/cm^3 [14] is impressively low in relation to the material's strength, making this an ideal option for a variety of industries to include medical, automotive, aerospace, pump parts, and much more [15]. The alloy is heat treatable, allowing for better mechanical properties. Al 4008 is a reliable choice because of its good ductility, strength, and corrosion resistant properties [16]. The Vickers hardness values for A356/Al 4008 alloy ranges from 60 to 105 HV [14]. A heat treatable aluminum alloy is capable of significant increases in strength and hardness due to precipitation hardening when exposed to higher temperatures (just below the material's melting point) [17]. A heat treatment consists of solution treatment, quenching, and aging and each step will be discussed in detail.

According to the printer manufacturer, "Printed Xerox® 4008 has a microstructure consisting primarily of silicon and AlFeSi distributed in an aluminum matrix. Two other phases, Mg_2Si and Al_3Ti, are stable at room temperature, although not resolvable or readily identifiable optically. High solidification rates associated with the ElemX process also produce a fine grain structure, which is typically cellular or columnar dendritic in nature, as compared with cast A356 material" [9].

C. QUENCHING

Quenching is rapid cooling of an object via submersion in water, or other cooling mediums, after being exposed to high temperatures. The intention of quenching is to "maintain the mechanical properties associated with…phase distribution that would be lost upon slow cooling" [18]. In liquid metal jetting, 3D printed parts are quenched immediately following completion of the printing process. A study on the effects of quenching rates was conducted by Seifeddine et al. showing a relationship between quenching rates and their effects on mechanical properties. Quench rates have a great "influence on the precipitation behavior in alloys A356…affecting mechanical properties" [19]. The precipitates mostly

affected by quenching rates are the silicon particles and less of the other intermetallic particles such as AlFeSi or Mg_2Si typically present in A356 [19]. Quenching a part has a very small window of time for when it is transferred from high temperatures to its quenching bath to maintain the desired outcome. For heat treatments, there is a 15 second window for the part to be taken out of the furnace and then quenched [20]. For the experiments the parts were quenched with water.

D. T6 HEAT TREATMENT

The T6 heat treatment process consists of solution treating, rapid quenching, and aging [21],[22]. For the parts printed using the ElemX 3D printer, the heat treatment's quenching is the second time the part will be quenched. T6 is a common heat treatment applied to Al-Si-Mg alloys to increase the hardness and strength of the material by precipitation of Mg_2Si particles [12]. Figure 6 illustrates the typical heat treatment process for aluminum alloys.

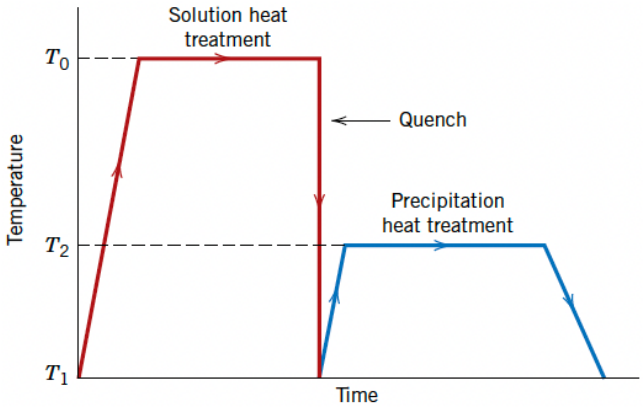

Figure 6. Heat Treatment Process: Solution Treatment → Quench → Precipitation Treatment. Source: [23]

The T6 heat treatment follows guidance provided by Xerox [24]. The ElemX 3D parts are noted to have a similar surface finish as sand casted parts allowing us to assume that the mentioned military specification is applicable for use on AM parts [5]. The parts were solution treated for 4 hours at 538 ºC and then immediately quenched. For parts that surpass 25.4 mm (one inch) in thickness, an additional 30 minutes of soak time is added for the

solution treatment and aging for every additional 12.7 mm (0.5 inch) increase [24]. Following the solution treatment and quenching, the part is aged for 3 hours at 155 ºC.

After T6 heat treatment, the reported A356/Al 4008 strength values by Xerox [24] are as follows:

- YS: 179 MPa for XY and Z Orientation
- UTS: 289 MPa for XY Orientation and 269 MPa for Z Orientation

1. Solution Treatment

The purpose of solution treating is to "produce a homogeneous solid solution with maximum solute concentration" [25]. Precipitates, or intermetallic particles, like are dissolved back into the Al-matrix in order to create a homogeneous solid solution [21]. Figure 7 shows the pseudo-binary phase diagrams concerning the concentration of silicon (AlSi7Mg) and magnesium (AlSiMg0.3). The solution treatment temperature is kept above the solvus temperature but below the liquidus temperature of the alloy. For aluminum alloys containing magnesium and silicon, the minimum solvus temperature is 270 ºC [26] which varies depending on chemical content. The melting point for AlSi7Mg0.3 alloy has been reported to range from 555 to 625 ºC [27]. The solvus temperature for the alloy used with the Xerox ElemX liquid metal printer is appreciably higher than 270 ºC, which drives the recommended solution treatment temperature of 538 ºC. At this temperature, silicon particles will form throughout the Al-matrix as shown in Figure 7. After solution treatment, the parts are quenched "to retain a high concentration of vacancies and solute in solid solution" [21].

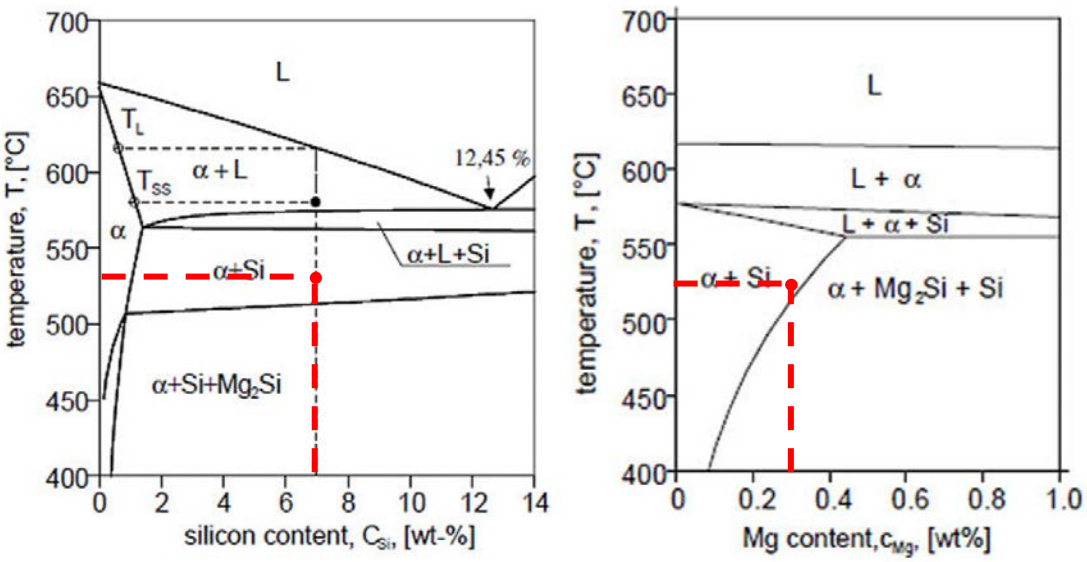

Figure 7. Pseudo-Binary Phase Diagram for AlSi7Mg (top) and AlSiMg0.3 (bottom). Source: [13]

2. Aging

Aging (also known as age hardening or precipitation hardening) is used to increase the strength and hardness of materials by having precipitates come out of the solid solution [20],[22]. Materials can be artificially or naturally aged. Natural aging occurs at room temperature for a long period of time and is sometimes limited in its effectiveness to precipitation harden. Artificial aging, specifically AlSiMg alloys, heats the part to 155 ºC for 3 hours to have similar or better effects than natural aging [12]. When aging Al 4008, the formation of Mg_2Si contributes to the improved hardness and strength. Other intermetallics that can be found in the Al-matrix include needle-like AlFeSi and Al_3Ti, but this paper will focus mostly on the precipitation of Mg_2Si and Si particles.

The primary strengthening precipitate (Mg_2Si precipitate) is developed from G-P zones [11]. The formation of precipitates from G-P zones help to explains how the increase in hardness is developed. To summarize, the formation of the Mg_2Si precipitate is as follows:

1. α-SSS
2. Si & Mg clusters
3. G-P zones

4. β”-phase
5. β’-phase
6. β-phase

The α-SSS is the supersaturated solid solution that occurs after solution treatment. From there, clusters of magnesium and silicon particles develop and eventually turn into G-P zones. As the aging process continues, the G-P zones evolve into metastable β”-phase precipitates then into β’-phase precipitates. Finally, the precipitates develop into the equilibrium β-phase [22], [28], [29], [30].

The phase that provides peak hardening characteristics is the metastable β”-phase. The equilibrium β-phase of Mg_2Si develops after overaging has occurred and the hardness and strength of the material decreases. Figure 8 diagrams the phase transformation of Mg_2Si and its relationship to the material's hardness or yield strength as aging time increases.

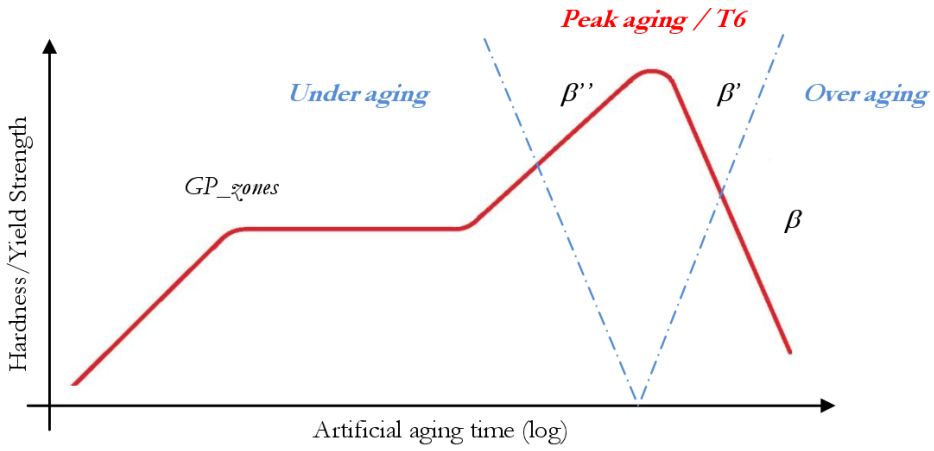

Figure 8. Primary Strengthening Precipitate (Mg_2Si) Formation During Aging. Source: [28]

The relationship between hardness, or strength, is explained by the increased lattice strains located at the G-P zones. Distortions develop due to the interaction between the Al-matrix and the precipitates forming. The distortions helps to prevent the formation of

dislocations within the material when deformed [23]. The continuing formation of the precipitate's equilibrium phase causes the material to be softer and weaker due to the lack of lattice strains between the Al-matrix and the precipitate's β-phase. Figure 9 shows the formation of the precipitate's phases as the aging process progresses, starting from SSS to its metastable phase and ending at its equilibrium phase.

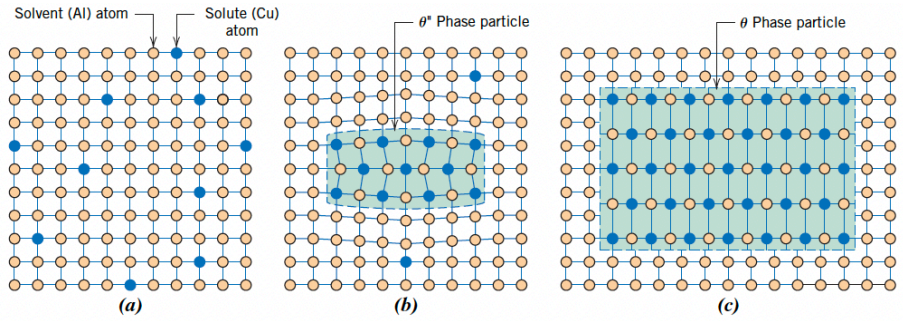

Figure 9. Precipitate Phases from G-P Zones to Equilibrium β-phase (Mg_2Si). Source: [23]

E. INERT GAS IN 3D PRINTING ENVIRONMENT

Aluminum is sensitive to the presence of oxygen where an "extremely small variation in oxygen content can impair the mechanical or chemical properties" [31]. Similar to concerns with welding, oxygen along with other reactive gases are not ideal to be in the atmosphere when 3D printing and the introduction of inert gas is necessary. Inert gas is chemically inactive and does not interact with the building properties of the 3D part. Air, though, is made up of mostly nitrogen but also oxygen, hydrogen, and carbon dioxide. Inert gases, such as argon or nitrogen, are introduced into the AM printing atmosphere to prevent air interacting with the printing projects [31].

The effects of air in the environment have been observed by Xerox while conducting tests on the ElemX printer. Xerox has reported gas porosity as a type of defect that might be observed and it is due to "dissolved hydrogen in [the] liquid aluminum" [9]. Along with the porosity issues in the 3D print, Figure 10 also shows the effects of oxidation between the layers.

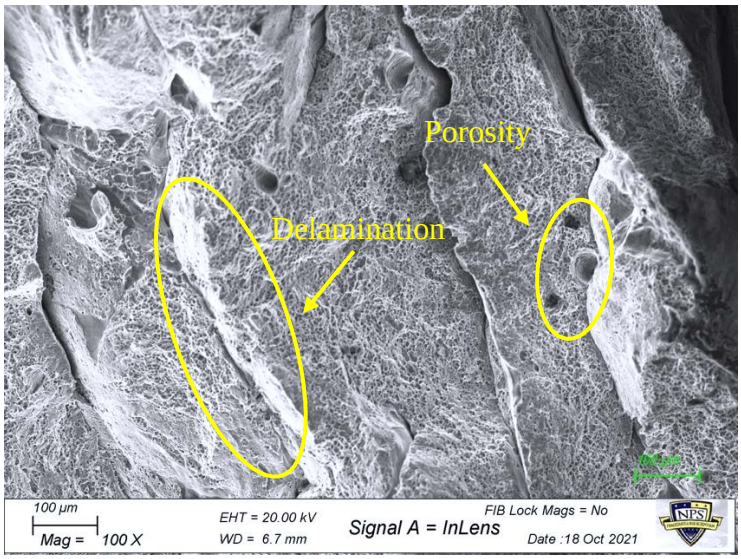

Figure 10. SEM Image of AM part with Delamination due to Oxidation and Porosity Locations

EOS and Linde studied the effects of oxygen concentration on the properties of the AM material, AlSi10Mg. They concluded that when AlSi10Mg was exposed to more than 1,000 ppm of oxygen, loss of density and mechanical properties could be observed [32]. Figure 11 depicts what a typical printing atmosphere consists of where argon makes up most of the atmospheric composition mixed with oxygen, nitrogen, carbon dioxide and hydrogen compounds. The effects of oxygen have been tested and proven to be detrimental in the 3D printing process, thus minimizing it is essential.

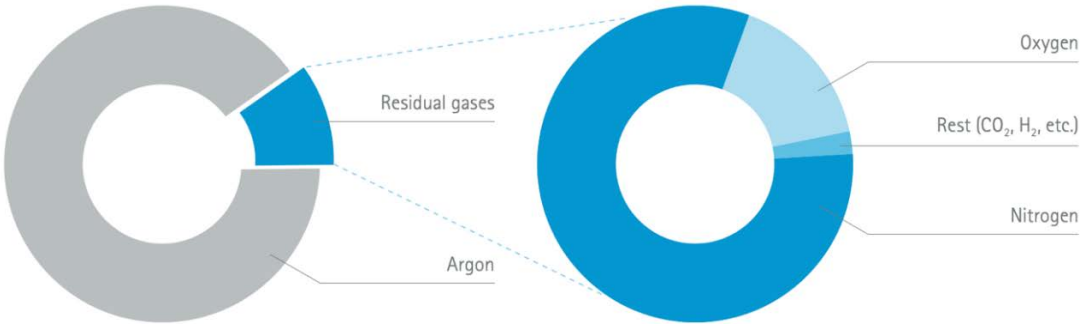

Figure 11. Composition of the AM Atmosphere. Source: [32]

F. THESIS OVERVIEW

The objective with these studies was to verify the optimal conditions to be employed in the post-printing processes of additively manufactured (AM) aluminum 4008 parts via liquid metal jetting. The influence of silicon (Si) and magnesium silicide (Mg_2Si) particle growth and size distribution within the aluminum matrix of the 3D parts, resulting from diverse quenching times as well as varying aging times and temperatures, was evaluated and compared to the resulting Vickers hardness data. Si particles are usually present in the aluminum matrix (Al-matrix) of Al 4008 after the first quenching operation upon removal of the 3D part from the printer, while Mg_2Si precipitates will appear after aging. Thus, the parametric study presented herein focused on the intermediate period between print completion to immersion into the quench bath and how delays influenced the part's hardness and microstructure. The results are compared to samples that were then solution treated to determine if the effects were reversed. Aging procedures were also evaluated as a continuation of the post-printing processes analysis. A variation of aging times and temperatures were tested to evaluate the applicability of A356 aging conditions on Al 4008 additively manufactured parts. In addition to post-printing process studies, an experiment to evaluate the effects of introducing additional argon into the printing environment during fabrication of the 3D parts to prevent oxidation and improve the prints quality was conducted. Argon is inert and helps decrease the detrimental effects caused by reactive gases existing in the air.

Initially, the hypothesis was that any delay to quenching upon completion of the 3D part will cause undesirable outcomes concerning hardness and microstructure but can be overcome with heat treatment regardless of how much time has elapsed for the intermediate period from print completion to immersion into quench bath.

Concerning the experiment on aging, as aging time or temperature increases, the part will experience overaging thus the hardness will suffer. If aging time or temperature decreases, the lack of exposure to the full aging effects will also cause a decrease in hardness.

As for the experiment concerning added argon in the print environment, the hypothesized outcome was that increasing the amount of argon will decrease the interaction with the reactive gases resulting in improved mechanical properties of the 3D parts fabricated.

Chapter II lays out the experimental methods conducted for each experiment and Chapter III discusses the results. Finally, Chapter IV will conclude all findings and discuss future studies that will support the findings made in this work.

II. EXPERIMENTAL METHODS

This chapter presents the methods utilized to analyze the effects of post-printing processes; quenching upon completion of the 3D print using the Xerox ElemX liquid metal 3D printer, and aging, in the properties of the specimens produced. An analysis on how quenching effects on a 3D print's mechanical properties change after increasing the intermediate period from when a 3D part is finalized at the 3D printer to the instant that it is introduced into the quenching bath was conducted. Analysis of mechanical properties include material hardness and microstructural effects after quenching as well as comparing the same samples to those that were solution treated.

Following, the chapter will then explain the aging procedure techniques employed to study the associated material hardness and examine the microstructures that resulted from using diverse times and temperatures. In addition, the chapter covers the procedures employed to design, fabricate, and test a gas delivery system meant to increase the amount of argon injected into the printing environment.

This chapter is organized into two parts: section A and B. The first part describes all the steps related to the study of quenching and aging conditions mentioned above, and their impact on material properties. The second part, section B, covers the procedures employed to evaluate the effects of argon addition to the printing environment in the material's yield and tensile strengths. Figure 12 portrays the different experiments conducted with reference to where they fall along the 3D part's process from as-printing to post-printing.

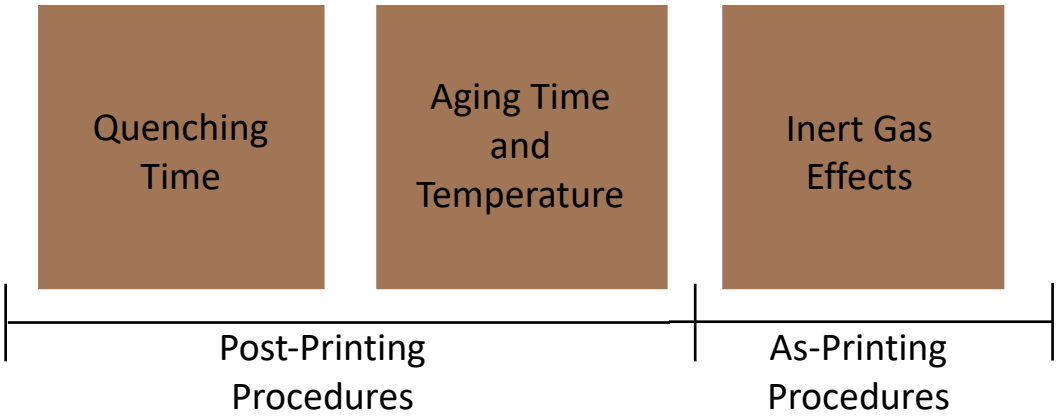

Figure 12. Experimental Topics Overview

A. POST-PRINTING PROCEDURES: QUENCHING AND AGING

1. 3D Printing Conditions

Prior to printing the 3D parts by the ElemX liquid metal printer, the parts were designed using a computer-aided design (CAD) program, such as SolidWorks, and started as an STL file. The STL file was imported into the slicer software provided by Xerox to generate a g-code file where the CAD model is "sliced" into layers and used as a guide for the 3D printer [33]. G-code is a programming language used by the 3D printer [34]. The G-code was then uploaded to the 3D printer. The ElemX heated the wire-fed Al 4008 in the printhead region up to 825 ºC and jetted from the nozzle onto the build plate heated to a target temperature of 475 ºC.

A simple cube design was used for both the quenching and aging experiments. Each cube measured, on average, 20.54 mm (0.81 inches) across all sides. Figure 13 shows one of those printed 3D cubes. All cubes are designed to be printed along the XY axis (horizontally printed). The material used to print the cubes was Al 4008 wire. The slicer's g-code was prepared to print six identical cubes in one print session.

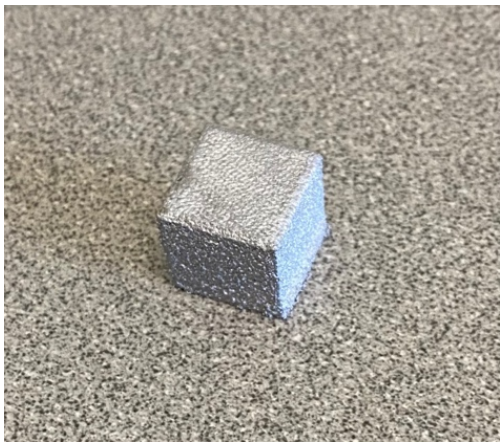

Figure 13. ElemX 3D Printed Cube

2. Quenching Effects Experiment

The experiment evaluates quenching delay effects by increasing the time it takes from print completion to introduction into the quench bath for each cube with six cubes total. At completion of printing, the build plate that the cubes were printed on remained in the ElemX printer. Typically, the build plate is removed from the printer using a crane and transferred to a quenching tank filled with water [35]. At one-minute intervals, the cubes were individually removed using tongs from the build plate and placed into a quench bath. Special consideration for the sitting time from completion of the prints to the start of the quenching procedure was minimized while still maintaining safety when working with equipment at elevated temperatures. The timer commenced at the placement of the first cube into the quench bath. Once all cubes were placed into the quench bath, the timer continued for an additional five minutes, and all cubes remained in place. All six cubes were then removed from the bath and dried. Figure 14 shows the cubes at completion of printing and then all six cubes in the quench bath. Figure 15 shows a diagram outlining the steps employed for the quenching effects experiment.

Figure 14. Cubes on Build Plate to Quench Bath

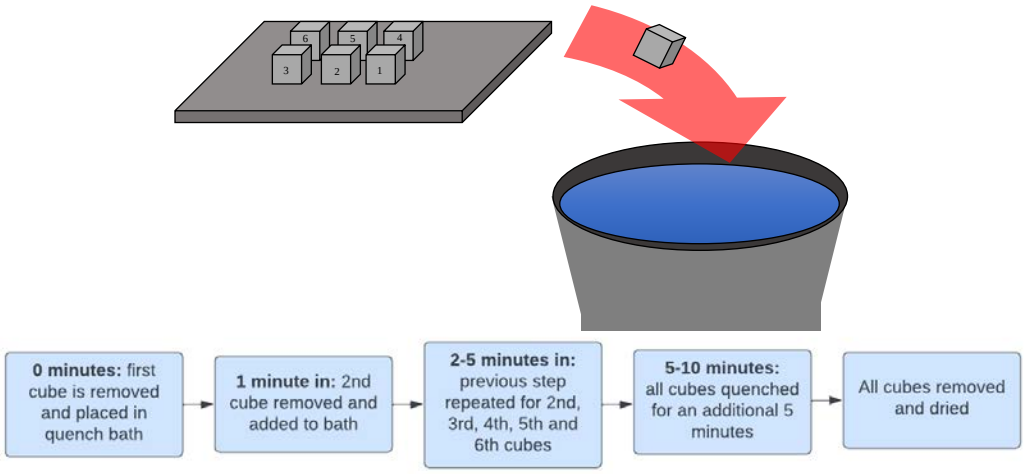

Figure 15. Diagram of Quenching Procedure

All 6 cubes were then cut in half along the Z-axis where one half each cube was analyzed for as-quenched effects and the other was analyzed for its effects after solution treating. For the solution treatment, the Thermo Scientific Lindberg/Blue M box furnace was set at 538 °C where the cube halves soaked for 4 hours and then immediately quenched in water at ambient temperature. For parts that surpass 25.4 mm (one inch) in thickness, an additional 30 minutes of soak time is added for the solution treatment and aging for every additional 12.7 mm (0.5 inch) increase [24].

A comparison of pre- and post-solution treatment effects were evaluated in hopes of overcoming any deficiencies caused by delay to quench. All cube halves, with and

without solution treatment, were placed and cured in epoxy using Struers EpoFix resin kit in preparation for polishing as pictured in Figure 16.

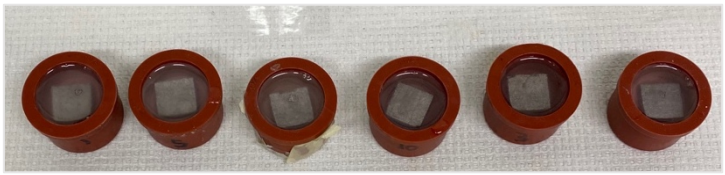

Figure 16. Cube Halves Curing in Epoxy

All samples, 12 in total, were polished and etched. Polishing was accomplished using the Buehler Ecomet 4 Polisher. The steps taken to polish the samples and their respective grit numbers are outlined in Table 2.

Table 2. Polishing Procedure

Step #	Grit #	Time (minutes)	Notes
1.	P1000	10	Repeat if epoxy remains on metal surface of sample
2.	P1500	15	---
3.	P2500	20	---
4.	P4000	30	---
5.	Polishing Pad	30	Al_2O_3 solution added at 0,10, and 20 minutes Distilled water added at 5 15, and 25 minutes

After polishing, all samples were etched using Keller's reagent on only half of the polished surface for each cube half. The orientation in which the etchant was applied covered half of the samples' XY-axis and spanned the entire length of its Z-axis. The reagent was swabbed on the surface for 10–15 seconds. The etching step specifically prepared the samples for OM and SEM. The samples were then tested for Vickers hardness.

The samples' surfaces were then observed using optical microscopy and scanning electron microscopy.

3. Aging Effects Experiment

The quenching procedure for the printed cubes followed the typical quenching process and all cubes were quenched identically. The cubes at completion of printing remained on the build plate and transported from the ElemX printer to the quenching tank and were submerged for one minute. The build plate was then removed from the quench bath and the cubes were promptly removed from the build plate. Figure 17 shows the steps taken to quench the 3D printed cubes.

Figure 17. Standard Quenching Procedure

All cubes were then solution treated at 538 ℃ for 4 hours in the Thermo Scientific Lindberg/Blue M box furnace and immediately quenched after in water. The cubes were then cut in half where one-half was stored and the other half were aged in the same furnace at various times and temperatures. Table 3 lays out the aging time and temperature for each sample with any variation from standard bolded and highlighted in red. The "A" prefix is for after aging indicating these are the samples relating to the aging effects experiment.

Table 3. Aging Temperatures and Times for Each Sample

Sample Code	Aging Variation	Temperature (℃)	Time
A155/A3	Standard	155	3 hours
A140	Low Temperature	**140**	3 hours
A170	High Temperature	**170**	3 hours
A2.67	Shortened Time	155	**2 hours 40 minutes**
A3.33	Extended Time	155	**3 hours 20 minutes**

Numbers represent aged temperature or time. Ex. 2.67 is 2.67 hours and 140 is 140 ℃.

The aging procedure of 155 ºC for 3 hours follows guidance provided by Xerox [24]. For parts that surpass 25.4 mm (one inch) in thickness, an additional 30 minutes of soak time is added for the aging procedure for every additional 12.7 mm (0.5 inch) increase [24]. For samples that did not follow standard aging procedures, either a 15 ºC or a 20-minute variation from standard was applied to assess their effects on the part's hardness and microstructure. After aging, the samples were polished and etched following the same procedures previously outlined.

4. Characterization and Testing

For both the quenching and aging experiments, all samples underwent hardness testing using the Vickers hardness method. For quenching affected samples, only a select few were imaged using OM and SEM/EDS while analysis was conducted on all the aging affected samples. For the quenching affected samples, the extreme samples were selected (the sample with no delay to quenching and the sample with the longest delay) as well as the sample with the most significant difference from the overall average. Further analysis will show the effects of increasing the intermediate period between printing and quenching at the microstructural level. Table 4 shows all the samples and the analysis conducted on each. The same samples chosen to conduct OM on were also used for SEM.

Table 4. Sample Codes and Testing Conducted

Sample Code	HV Testing	OM Imaging	SEM Imaging
Q0	X	X	X
Q1	X	---	---
Q2	X	---	---
Q3	X	---	---
Q4	X	X	X
Q5	X	X	X
S0	X	X	X
S1	X	---	---
S2	X	---	---
S3	X	---	---
S4	X	X	X
S5	X	X	X
A155/A3	X	X	X
A140	X	X	X
A170	X	X	X
A2.67	X	X	X
A3.33	X	X	X

Q = After Quenched S = After Solution Treated A = After Aged. For samples denoted Q or S, the number represents the delayed time until quenched in minutes. For samples denoted A, the number is referring to its aged temperature or age time.

a. Vickers Hardness (HV) Testing

The hardness of the 3D parts was evaluated using Vickers hardness. Vickers hardness makes a "square-based pyramid" indent into the surface of the material to measure hardness. The hardness value, or HV, is calculated using the following equation [36]:

$$HV = 1.854(F/D^2)$$

The force is an "applied load" in kg-force that the indentor will put onto the surface of the material. The applied load is represented by, for example, HV0.1. A reported Vickers hardness will be presented with its value following with HV (i.e., 150 HV). If the applied load is also being reported with the hardness value it will look like: 150 HV0.1 [37]. The area of the indent is calculated by squaring the diameter (in mm) that is measured from opposite corners of the square [36].

The Struers Inc. DuraScan was used to conduct Vickers Hardness testing on all samples. Figure 18 shows a typical hardness test point. The sample was placed on the DuraScan platform, and each cube was tested along two different axes, Z- and XY-axis, with 20 points in each direction. The Z-axis, or Z-points, started from the bottom of the sample where the first layer is printed and ends at the top where the last layer was printed and is at the center of the surface. Figure 19 diagrams the testing points orientations. This orientation showed the pattern of hardness and how it changed as the print progressed as the layers build. The XY-axis, or XY-points, runs from left to right along the center of the surface. The XY-points were used to compare the Z-points to ensure accuracy. The discussion of results focuses on the Z-points to report hardness as it covers various layers of the print giving a thorough understanding of the part's hardness as layers were built.

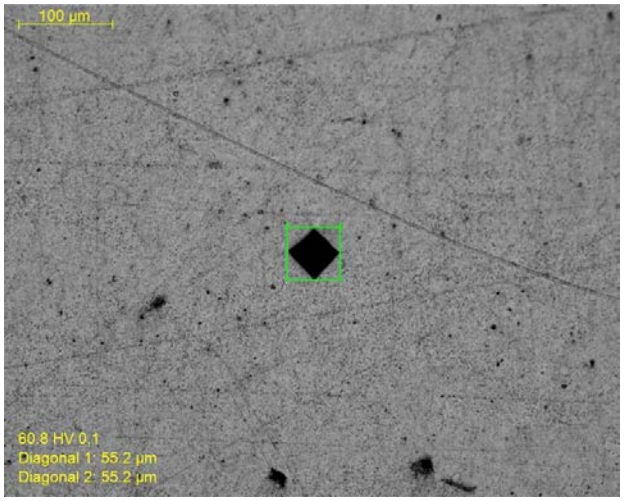

Figure 18. Vickers Hardness Test Point

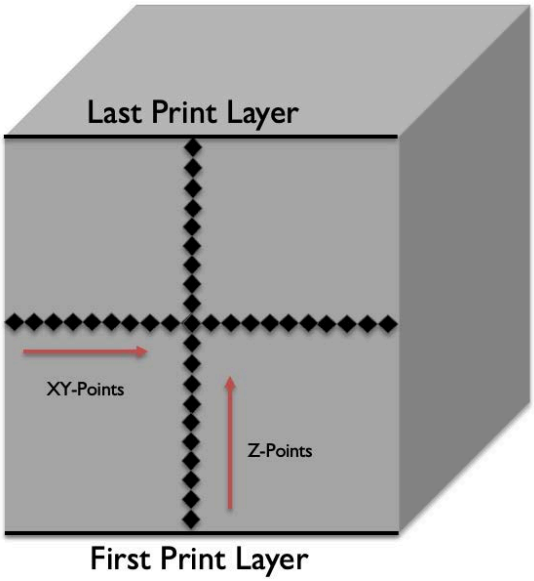

Figure 19. HV Testing Points Orientation

HV0.1 load was chosen so that more points can be captured, resulting in more layer variation along the Z-axis. HV0.5 load results was compared to HV0.1 load to determine accuracy. The results were similar indicating that HV0.1 load accurately captured the hardness characteristics of each sample.

b. Optical Microscopy

The Nikon Epiphot 200 was used to capture optical microscopy images at 2.5x, 10x, 20x, 50x, and 100x magnification. OM images capture the expected phases present, grain sizes, pores and other microstructural features such as defects. The size of particles was measured to relate the HV results to the average Si particle sizes.

c. Scanning Electron Microscopy

The ZEISS Neon 40 was used to capture SEM images. The goal with SEM imaging was to generate images of the microstructural features at higher magnification, resolution and contrast. This allows for better imaging to see the varying sizes of the particles present in the Al-matrix. ImageJ was used to help evaluate the changes in Si particle sizes between each sample. ImageJ is a measurement tool publicly available that

uses pixel counts that, for this research, was used to measure particle sizes [38]. The pixel count is set to a scale specific to each SEM image.

B. ARGON ADDITION IN PRINTING ENVIRONMENT

Our experiment focusing on solving the oxidation issue causing delamination between layers was conducted by adding inert gas to the printing environment, specifically argon. The ElemX printing system was designed with argon already flowing into the printhead region. The device coined the argon injector was designed, fabricated, and tested to aid in analyzing the effects of added argon in the printing environment. The prints were analyzed for changes in yield and ultimate tensile strength as well as changes in microstructure.

1. Argon Injector Design

The argon injector was designed in the SolidWorks CAD program and to be printed using the ElemX 3D printer with wire-fed Al 4008. The design of the argon injector needed to be easily installed so that it did not require any major alterations to the current state of the ElemX 3D printer. The injector was designed to easily attach to the printhead platform surrounding the jetting nozzle dissipating argon directly at the jetted droplets of the liquified metal. Argon was fed to the injector by a line from an outside source at a flowrate of 8.48 SLPM. The flow of argon from the injector needed to not cause any bending of the jetting stream, which would negatively affect the 3D part's mechanical properties.

Figure 20 shows the SolidWorks design of the argon injector. The figure identifies where the argon was fed into as well as the internal design of the diffuser portion. The diffuser was designed with guide vanes with an opening to direct the argon flow on to the jetted stream of the liquid metal droplets.

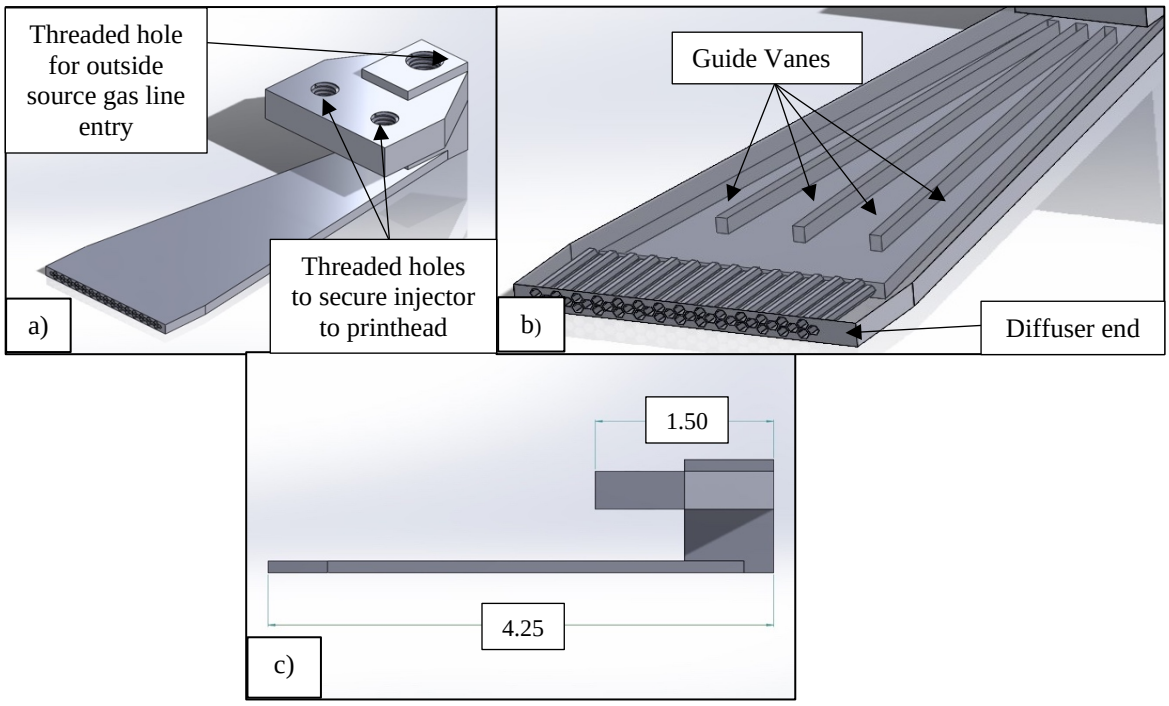

a) 3D view of injector. b) cut away view of guide vanes and diffuser end. c) side view with dimensions.

Figure 20. Gas Injector SolidWorks Sketch (dimensions in inches).

The diffuser measures 108 mm (4.25 inches) in length and 38.65 mm (~1.52 inches) wide. The measurements allow for a 19 mm (¾ inch) gap between the center of the jetting stream outlet to the injector to prevent the extreme heat surrounding the nozzle does not melt the injector. Figure 21 shows the jetting outlet with a FLIR image to highlight the increased temperature at that location.

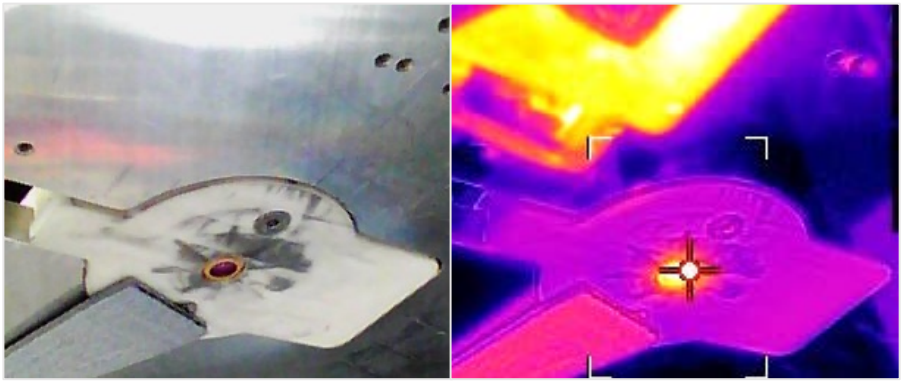

Figure 21. Jetting Outlet Compared to FLIR Image

The design for the argon injector also considered the build plate's temperature (up to 475 ºC) and ensured no direct interaction with the build plate. The thickness for the diffuser section of the argon injector is 3.25 mm (~0.128 inches). The thickness of the diffuser end prevented direct interaction with the build plate. If the injector contacted the build plate, the printer would give an error notification and would stop printing the part. Figure 22 shows the diffuser end with the rectangular openings.

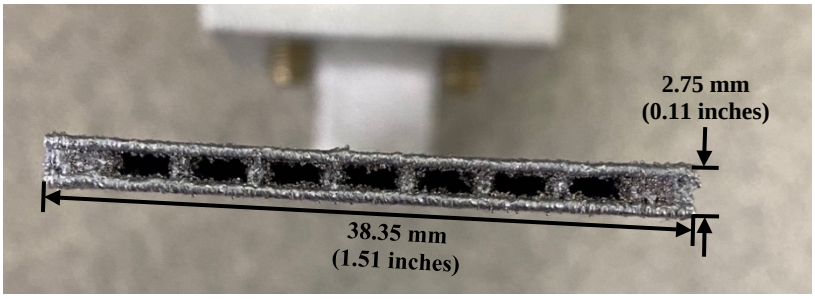

Figure 22. Argon Injector Diffuser End

Each individual rectangular opening measures 1.75 mm (~0.07 inches) high and 4 mm (~0.157 inches) in length. The wall thickness of the diffuser section and for the guide vanes measures 0.68 mm (0.0268 inches).

2. Fabrication of Argon Injector

The part was printed using the Xerox ElemX 3D printer in a standard printing environment followed by standard quenching procedures. The measurements of the argon injector challenged the ElemX printer. The Xerox recommended minimum threshold for hole size and wall thickness is 3 mm [39]. Although the minimum threshold was surpassed, the outcome was impressively successful. Figure 23 shows the printed argon injector.

Figure 23. Argon Injector 3D Printed by ElemX

3. Argon Injector Integration into ElemX 3D Printer

Figure 24 shows the set-up and the placement of the argon injector on the ElemX 3D printer. The argon injector was designed to be installed next to the jetting stream and attaches to the printhead.

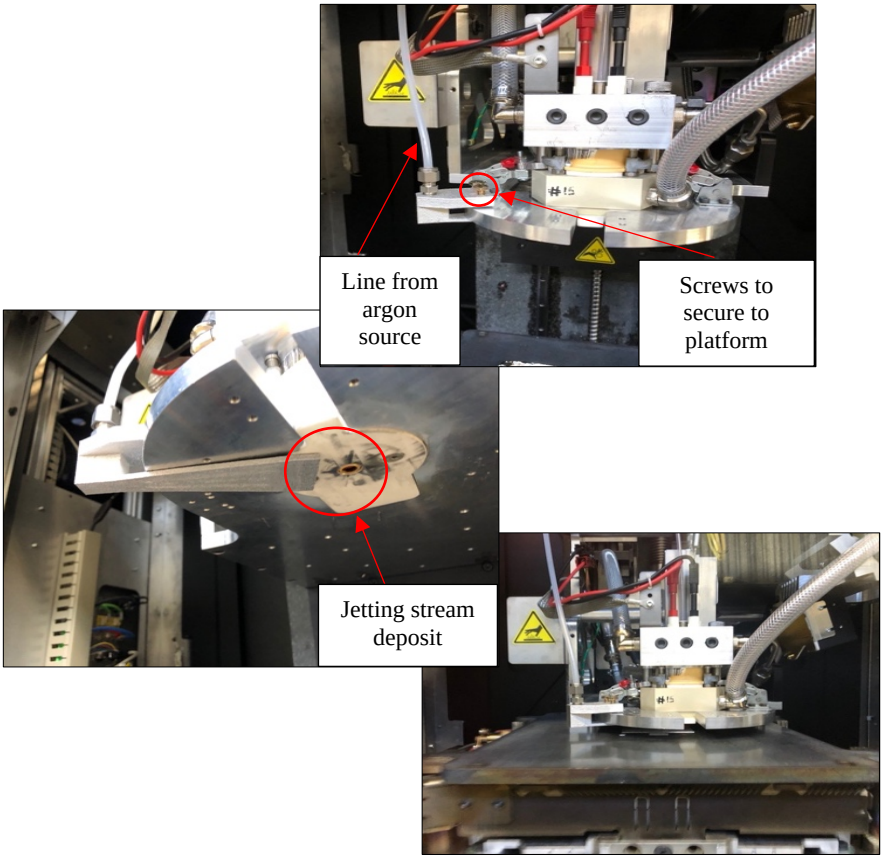

Figure 24. Argon Injector installed onto XEROX ElemX Printer Printhead

4. 3D Printing Conditions

A standard printing environment is one in which the target temperature for the nozzle is 825 ºC and for the build plate is 475 ºC. The standard argon flowrate for the ElemX 3D printer is nominally 7 SLPM. The same process of uploading part designs into the 3D printer were implemented. The standard post-printing quenching procedures were followed for this experiment.

For the added argon environment, adjustments were made to the overall flowrate of argon being introduced to the environment. The argon flowrate increased from 7 SLPM to 15.48 SLPM where 8.48 SLPM was provided by a device coined the argon injector. An outside source of argon was connected to the argon injector by a hose that fed into the printing environment from an access point located above. The argon injector

was installed onto the printhead region where the diffuser was directed right at the jetting stream located just below the nozzle.

The print design used for this experiment was a rectangular block The shape is ideal to machine three circular tensile specimens in accordance with ASTM E8 size standard from each block. A single block was printed in a standard gas environment and in an added argon environment. Figure 25 shows a printed block.

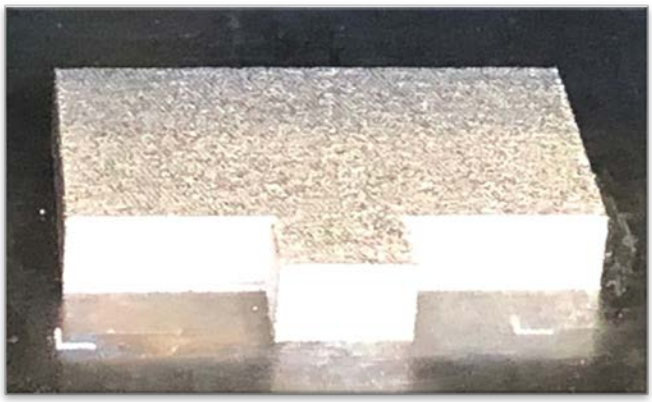

Figure 25. Block Design on ElemX Build Plate

5. Characterization and Testing

a. Tensile Testing

The tensile specimens from their respective blocks were tensile tested to failure using the 5982 Instron mechanical testing system. Each block had three tensile specimens machined and tested. The rate at which the specimens were tested at was 2 mm/min. The tensile test setup is pictured in Figure 26 prior to and after testing the circular tensile specimens to failure.

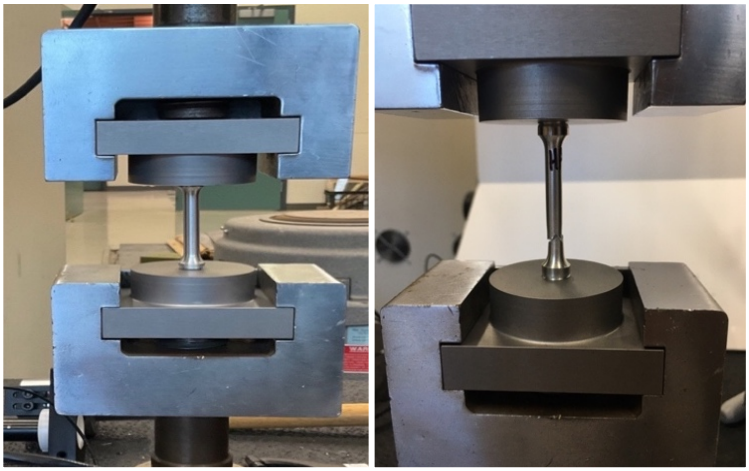

Left: Tensile Specimen prior to commencing tensile test. Right: Fractured Specimen upon completion of tensile test.

Figure 26. Before and After Conducting Tensile Test

b. Scanning Electron Microscopy

After tensile testing, the specimen's failed surface was cut and analyzed using the FEI Inspect F50 SEM and the ZEISS Neon 40 for EDS analysis. SEM provided images of any surface impurities including delamination of the layers, contaminants in the print, and porosity.

c. Optical Microscopy

An additional piece was cut from the specimen for OM imaging. The cut tensile specimen piece was prepared in epoxy for polishing. The same polishing steps were followed as previously outlined. The sample was etched using Keller's reagent prior to taking OM images. The results of the standard and added environment specimens were compared for any changes in contaminants, porosity, and delamination.

THIS PAGE INTENTIONALLY LEFT BLANK

III. RESULTS AND DISCUSSION

A. POST-PROCESSING PROCDECURES EXPERIMENTAL RESULTS

This section discusses the results from the experiments conducted on post-printing processes. The first section covers the results from the quenching experiment. This experiment evaluated the effects of increasing time from print completion to immersion in the quench bath. Next, this section covers the results from the aging experiment and the effects of diverse times and temperatures on the part's mechanical properties. For both experiments, the results from the Vickers hardness test, OM, and SEM analysis are discussed.

1. Quenching Variation

a. Vickers Hardness Test Results

The results of the Vickers hardness test are reported using the hardness test points taken in the Z-direction, or Z-points. The results of the Vickers hardness test in the XY-direction rendered similar trends to the results in the Z-direction and can be found in the Appendix. Hardness test points taken in the Z-direction gives a more accurate idea of how hardness varies as the 3D part was built layer by layer. Figure 27 displays the results of the as-quenched cubes and their related Vickers hardness values as box-and-whisker plots. The variation in HV ranges from 51.6 to 64.3 HV with the average being 59.82 HV. The sample with no quenching delay (Q0) reported the highest average hardness at 60.71 HV while the sample with a 4-minute delay to quenching (Q4) has an average hardness of 58.08 HV. There appears to be a downward trend in the hardness values as the quenching time increases with the sample Q5 being an exception.

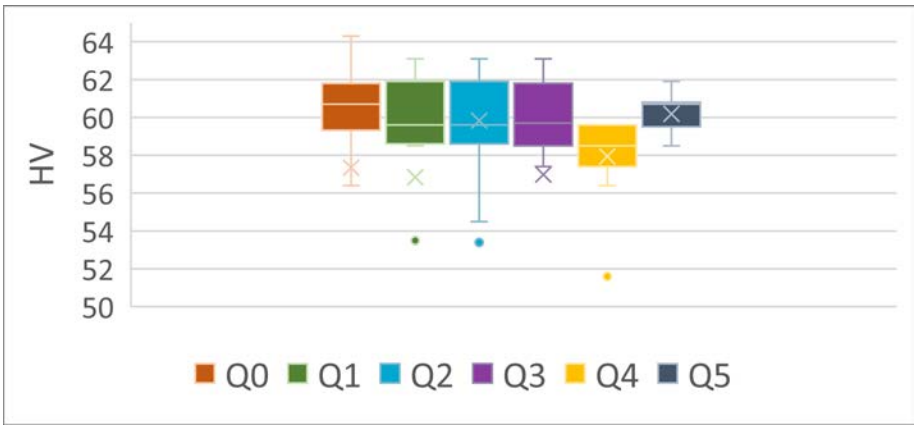

Figure 27. Box-And-Whisker Plots of As-Quenched HV Results

Solution treatment of the same samples increased hardness by an average of 22 HV; a 36.42% increase. Figure 28 shows the hardness for S0, the sample that was quenched immediately following print completion, is significantly greater than the rest of the samples by 6.67% from the average 81.36 HV. This indicates that there is a critical time of less than one minute for the intermediate period leading to quenching before causing changes to the microstructure that cannot be reversed by the prescribed solution treatment. After this critical time, the effects of the quenching delay on the hardness of the 3D parts are minimal in comparison to one that experienced no delay.

The Q4 sample originally showed significant lowest average hardness than the other samples. After solution treatment, the S4 sample increased in hardness to a similar extent than other samples that experienced a delay of more than one minute, with only a 0.2971% decrease from the average of 80.28 HV. Though a critical time was observed to achieve optimal hardness (one minute), solution treatment can still reverse the detrimental effects from delay in quenching as seen with the results of S4 but to a certain threshold. It is worth noting that the values presented herein represent an average of approximately 20 points taken for each sample.

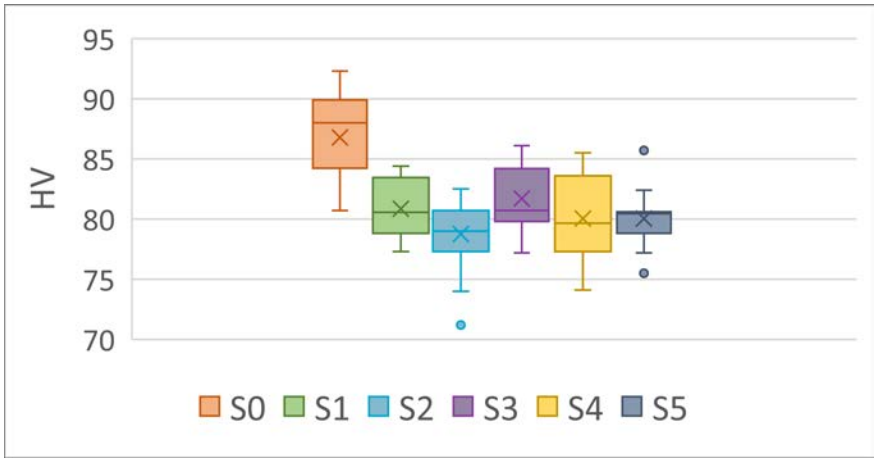

Figure 28. Box-And-Whisker Plots of Solution Treated HV Result

Average HV As-Quenched vs Quench Delay Time Figure 29 and Figure 30 shows point-to-point hardness testing results for as-quenched and after solution treatment samples. The plots show the results with no delay (Q0 and S0), 4-minute delay (Q4 and S4), and 5-minute delay (Q5 and S5) to quenching. The as-quenched HV results shows a consistent lower HV value for the 4-minute delay with a considerable drop at point 13. Conversely, after solution treatment the S4 sample shows a similar trend to the S5 sample. The effect of the solution treatment is pronounced when comparing hardness results of samples before and after solution treatment and shows it was effective in reversing significant defects due to delay to quenching. The drop in HV values in the middle of the values is consistent with a slower cooling rate due to the thickness of the sample as the specimen is quenched.

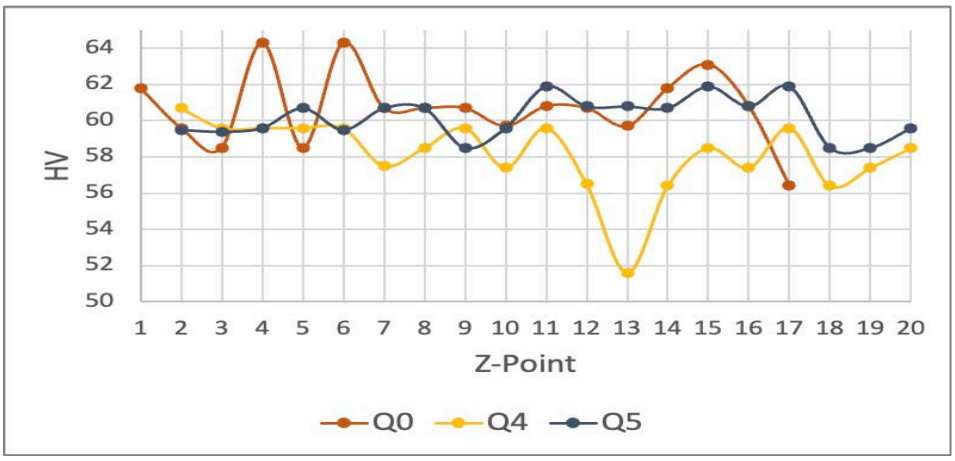

Figure 29. As-Quenched Point-to-Point HV Results Along Z-Direction

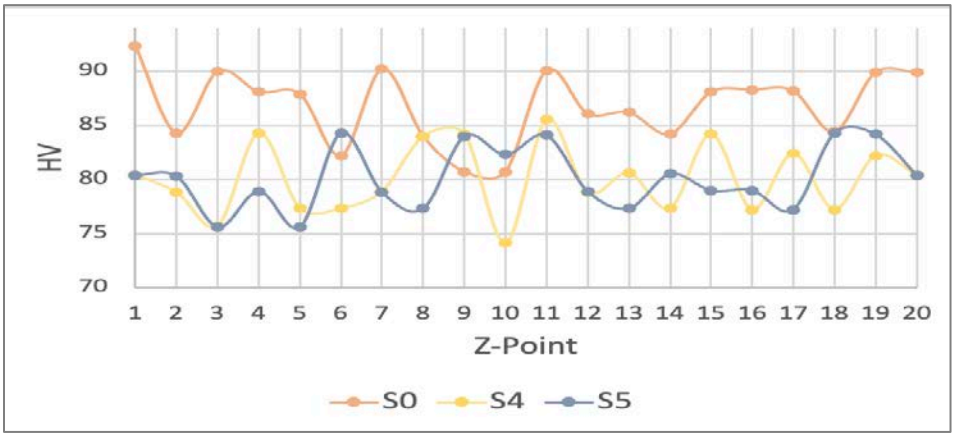

Figure 30. After Solution Treating Point-to-Point HV Results Along Z-Direction

b. Optical Microscopy Analysis

The purpose of solution treatment is to dissolve intermetallic particles, like Mg_2Si, back into the Al-matrix. This allows an opportunity to reverse any effects caused from the time delay to quench. At 538 ºC, as previously discussed in Figure 7, not all Si particles are dissolved back into the Al-matrix but instead continue to grow and contribute to the increased hardness of the material. Figure 31 through Figure 33 shows OM images at 100x magnification of as quenched and after solution treatment samples. Specifically, the images show samples with no delay (Q0, S0), 4-minute (Q4, S4) and 5-minute delay (Q5, S5). An increase in size for the Si particles are significant.

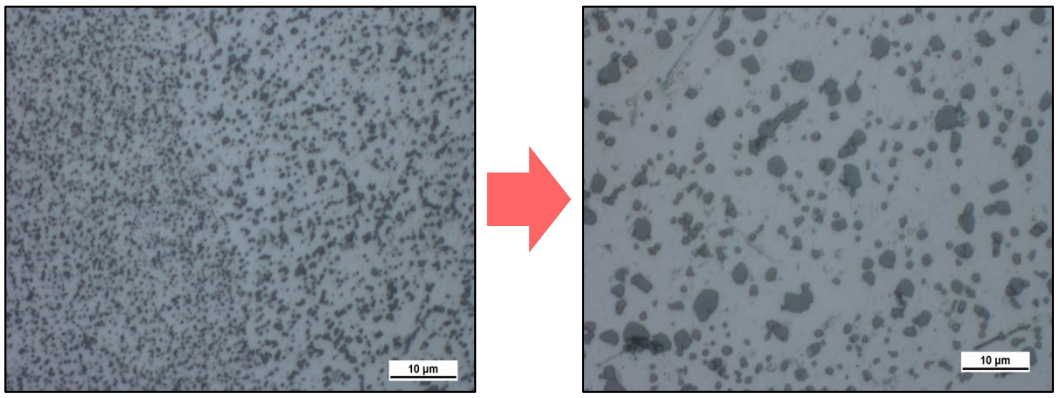

Figure 31. OM Images of Q0 (left) and S0 (right)

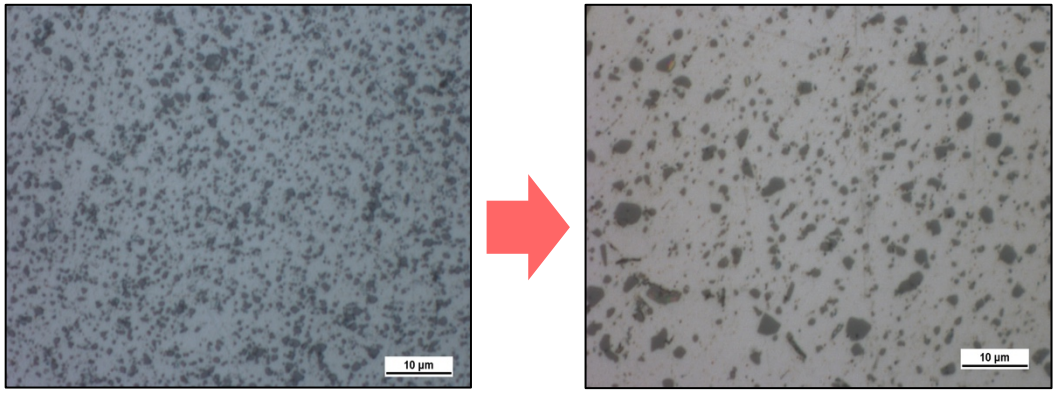

Figure 32. OM Images of Q4 (left) and S4 (right)

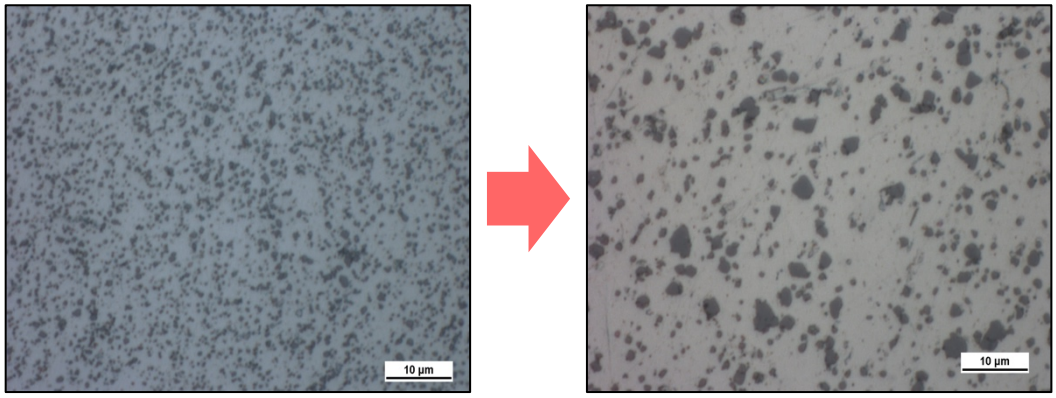

Figure 33. OM Images of Q5 (left) and S5 (right)

c. Scanning Electron Microscopy & ImageJ Analysis

(1) SEM Imaging

SEM images at 5,000x magnification show similar results as the OM images. Figure 34 through Figure 36 shows the increase in Si particle sizes from as quenched to after solution treatment for the same samples as analyzed using OM.

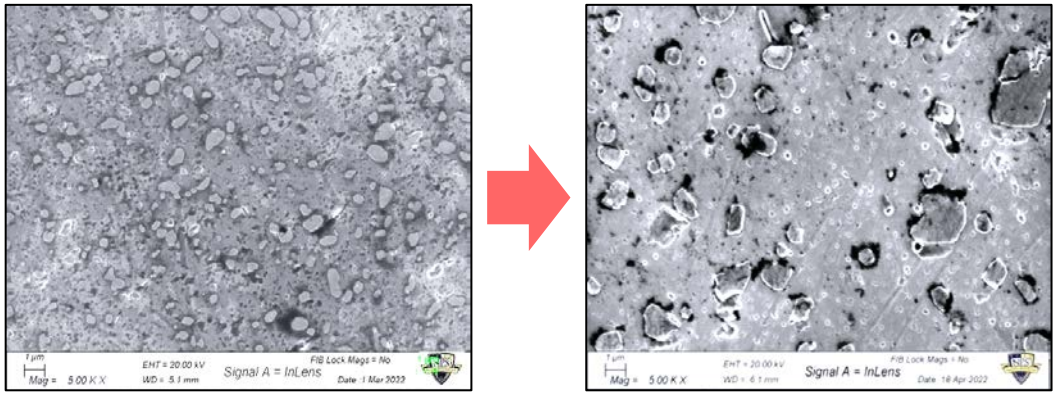

Figure 34. SEM Images of Q0 (left) then S0 (right)

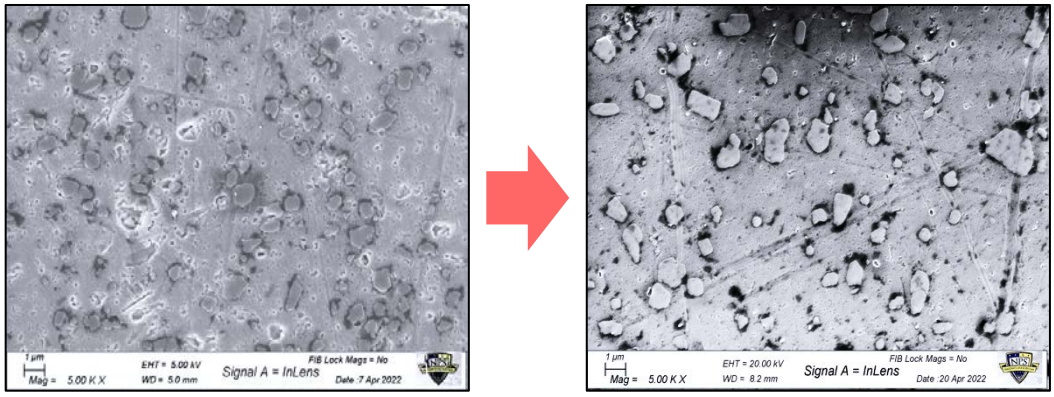

Figure 35. SEM Images of Q4 (left) then S4 (right)

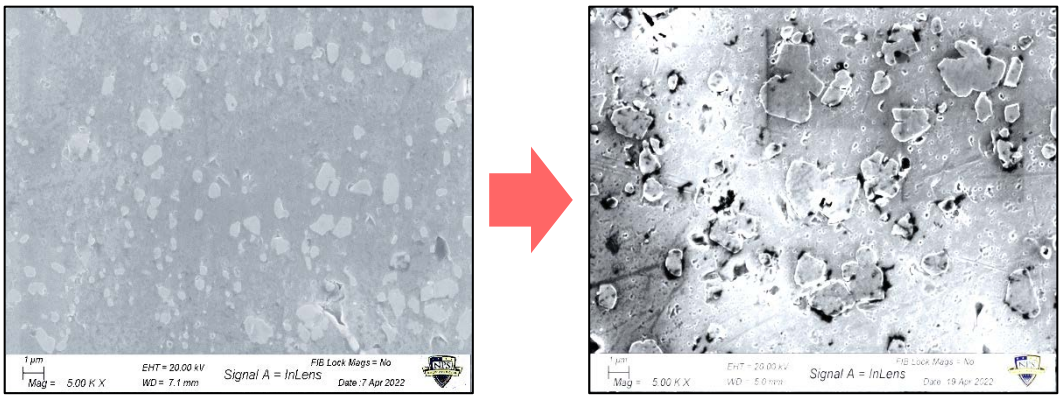

Figure 36. SEM Images of Q5 (left) then S5 (right)

(2) ImageJ - Si Particle Size Distribution Analysis

Since SEM can achieve higher magnifications, images at 1,000x and 5,000x magnification were captured and used to count the Si particles present in the Al-matrix using ImageJ. Each particle's length was related to the image's scale. All as-quenched images used 5,000x magnification to count particles while "after solution treated" images used 1,000x magnification. The reason for this is the particles are too spaced out in the "after solution treated" SEM images to collect enough particles in one image. Figure 37 shows an SEM image in ImageJ with all the particles measured indicated by a yellow solid line.

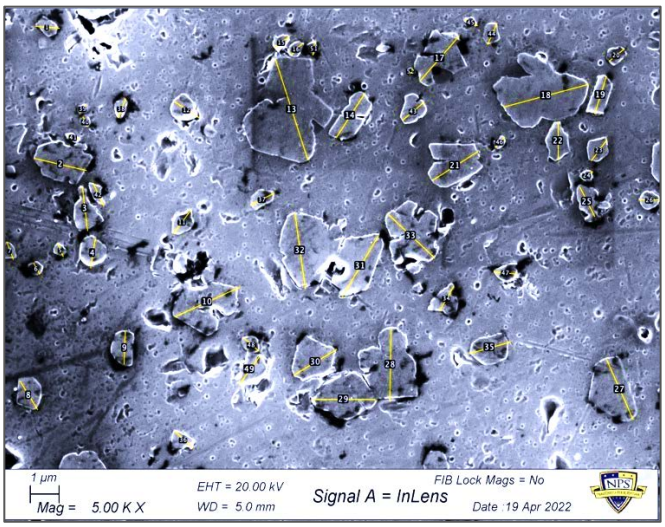

Figure 37. SEM Image at 5,000x Magnification With Measured Particles Using ImageJ

Figure 38 shows the results of Si particle size distribution for all samples measured. Table 5 and Table 6 report each sample's mean, median and mode. The Si particle sizes within the Al-matrix increased by 107.8% on average after solution treatment for all samples tested. This is typical of A356/Al 4008 behavior after solution treatment and contributes to the increased hardness [40]. Before solution treatment, the size of Si particles in the 4-minute delay sample (S4) were, on average, the largest by 13.36% compared to the other samples tested. After solution treatment, the same sample's average size of the Si particles were the smallest by 15.21% compared to the other samples.

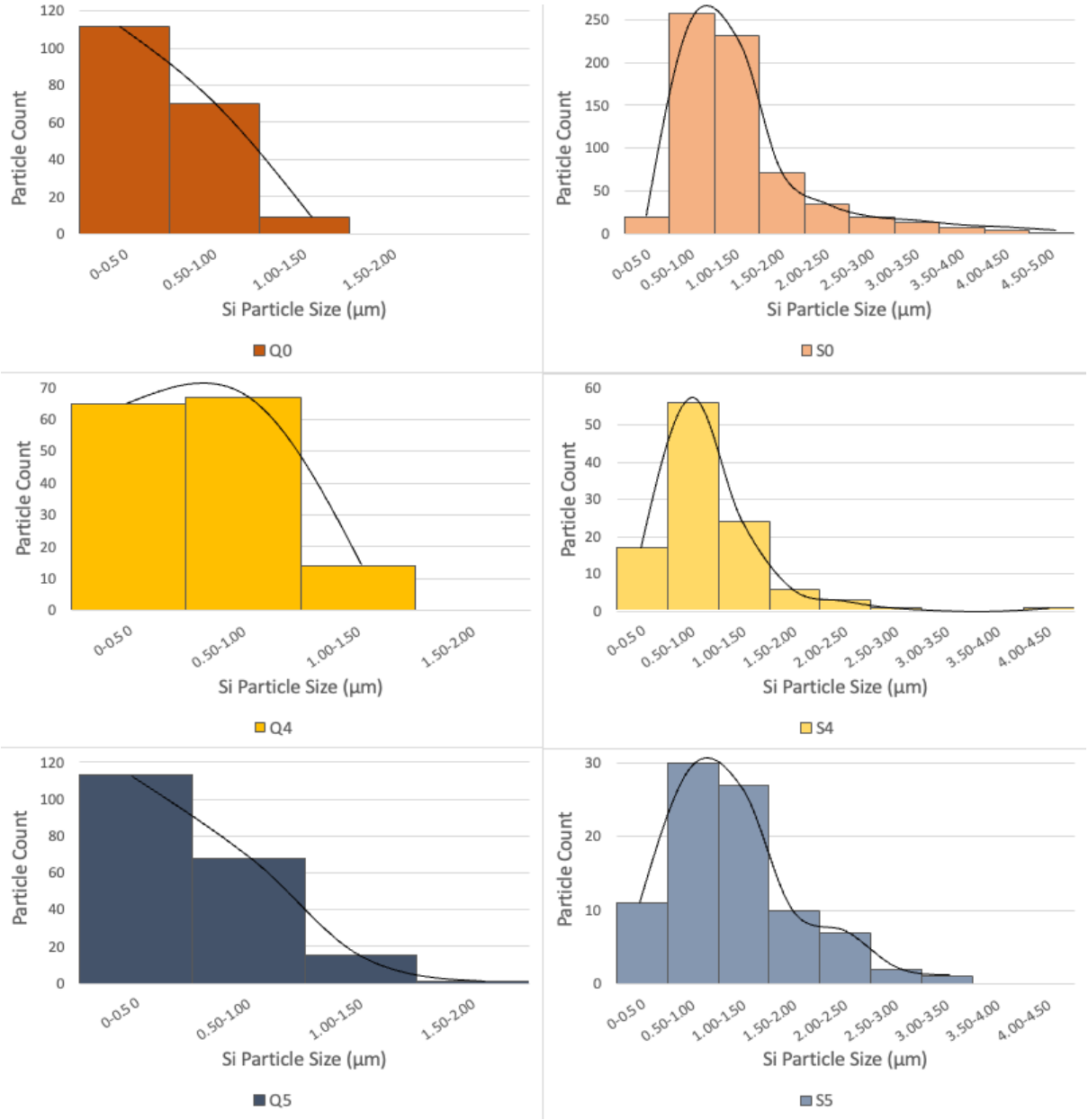

Figure 38. Si Particle Size Distribution Plots for Q0 & S0, Q4 & S4, and Q5 and S5

Table 5. As-Quenched Quantitative Characteristics of Si Particle Size Distribution

Sample Code	*Si mean length (µm)*	*Si median length (µm)*	*Si mode length (µm)*
Q0	0.509	0.464	0.370
Q4	0.611	0.575	0.276
Q5	0.498	0.437	0.293

Table 6. Solution Treated Quantitative Characteristics of Si Particle Size Distribution

Sample Code	*Si mean length (µm)*	*Si median length (µm)*	*Si mode length (µm)*
S0	1.27	1.08	0.929
S4	0.953	0.799	0.502
S5	1.15	1.03	1.10

A possible explanation for this observed behavior is by Ostwald ripening. As depicted in Figure 39, the Ostwald dissolution mechanism [41] states that smaller Si particles are “diluted and diffused” into the Al-matrix while larger Si particles remain and continue to grow in size. Thermodynamically, larger particles are more energetically favorable in comparison to the smaller particles that were dissolved. Since, on average, the Si particles for the Q4 sample show to be larger, less silicon was dissolved back into the Al-matrix thus leaving less available silicon amount to increase the sizes of existing Si particles during solution treatment. The increase in Si particle sizes contributes to the strength and hardness of the material and the results have proven this.

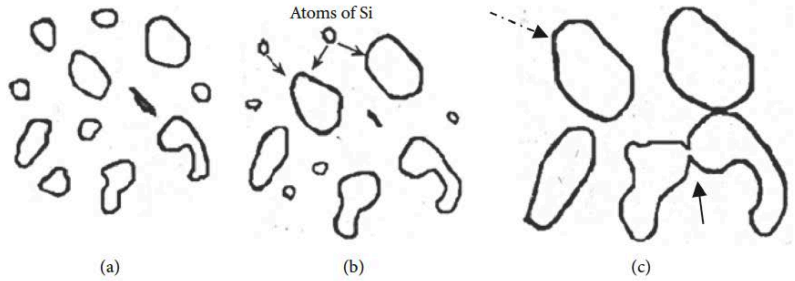

Figure 39. Schematization of Ostwald Dissolution Mechanism. Source: [41]

A study by Shuhui Ma [42] showed similar behavior concerning Si particle growth when various quenching rates were used prior to aging. A faster quenching rate resulted in larger Si particles while a slower quenching rate caused smaller Si particles to grow. This study's results are comparable because the samples that experienced a delay to quenching is like a slower quenching rate.

2. Aging Temperature and Time Variation

The next experiment evaluated varying aging times and temperatures and their effects on hardness and microstructural features of the 3D parts. For AlSiMg0.3 at temperatures below 200 ºC, the main phases that will be present in the Al-matrix are Si and Mg_2Si. The presence of β"-Mg_2Si is predicted to improve the strength and hardness of the material. Figure 40 shows the pseudo-binary phase diagram with the red dotted line indicating 0.3 wt% Mg.

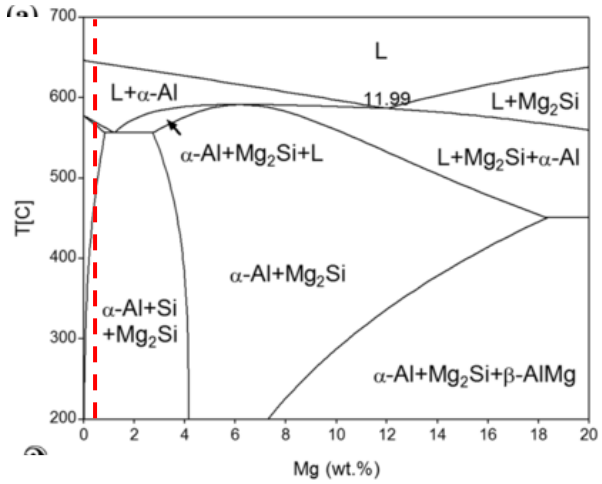

Figure 40. Pseudo-Binary Phase Diagram of AlSiMg0.3. Source: [43]

a. Vickers Hardness Analysis

(1) Aging Temperature Variation

Various aging temperatures with a constant aging time of 3 hours for all samples were analyzed. The temperatures tested were 140 ºC (A140), 155ºC (A155), 170ºC (A170) As shown in Figure 41, varying aging temperatures show a gradual increase of 1.87% from the A140 sample to the A170 sample. The trend shows that as temperature increases, HV increases as well. The formation of Mg_2Si starts to overage when the β”-phase develops into β’-phase. As depicted in Figure 8, the phase transformation of Mg_2Si into β’-phase will start to experience a decline in hardness. For this part of the experiment, overaging was not reached indicated by the continual hardness increase with increasing aging temperatures.

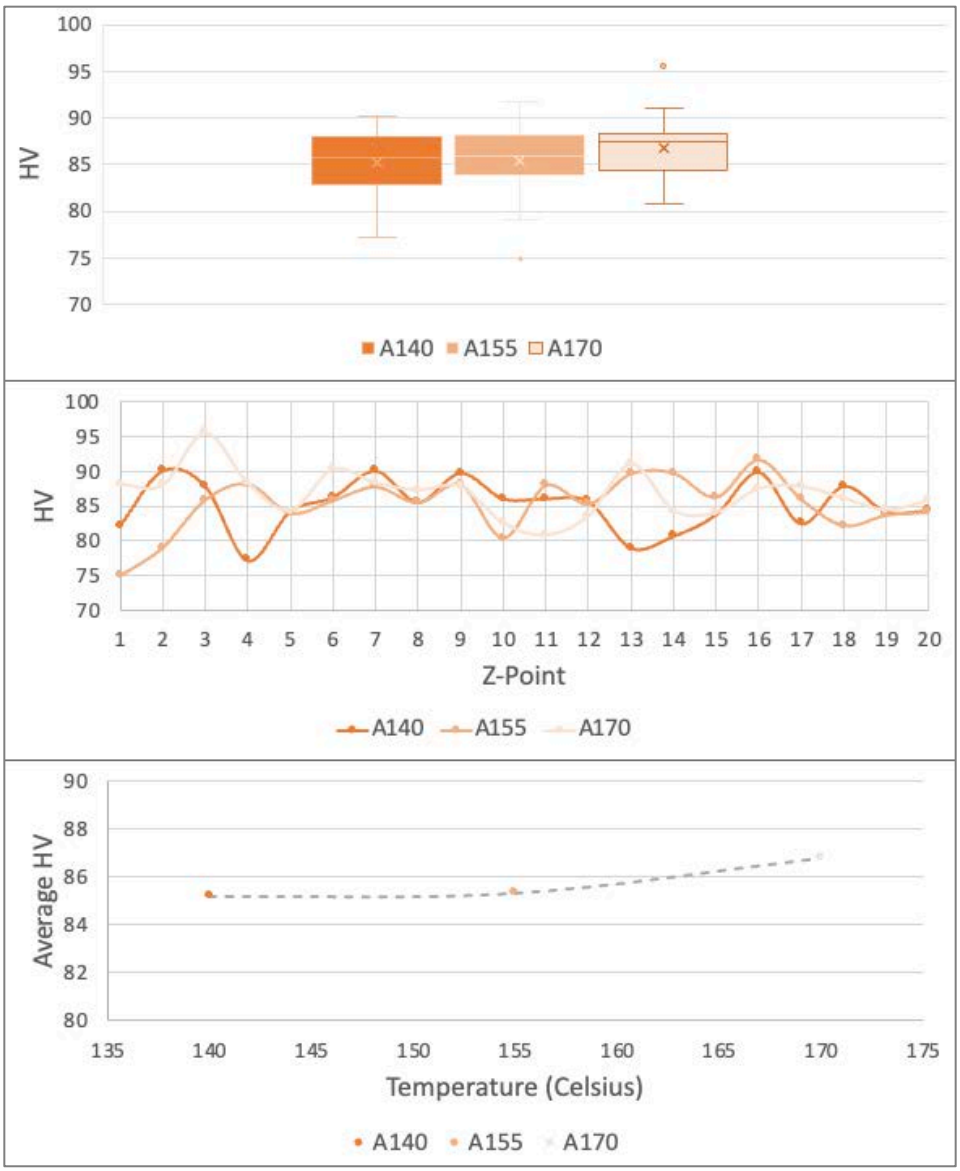

Figure 41. HV Results for Variation in Aging Time

(2) Aging Time Variation

Varying aging times with constant aging temperature at 155ºC was also tested. Like the results from the varying aging temperatures, varying times shows a 2.28% increase in HV with increased aging time as depicted in Figure 42. Overaging, again, is not a concern at these times because of the continual increasing trend. Though a slight decrease in the average HV is recorded from A2.67 to A3, this is not substantial to show that overaging

was reached. This is supported by an increase in HV from A3 to A3.33. If overaging was reached, a continual decline in hardness would be observed.

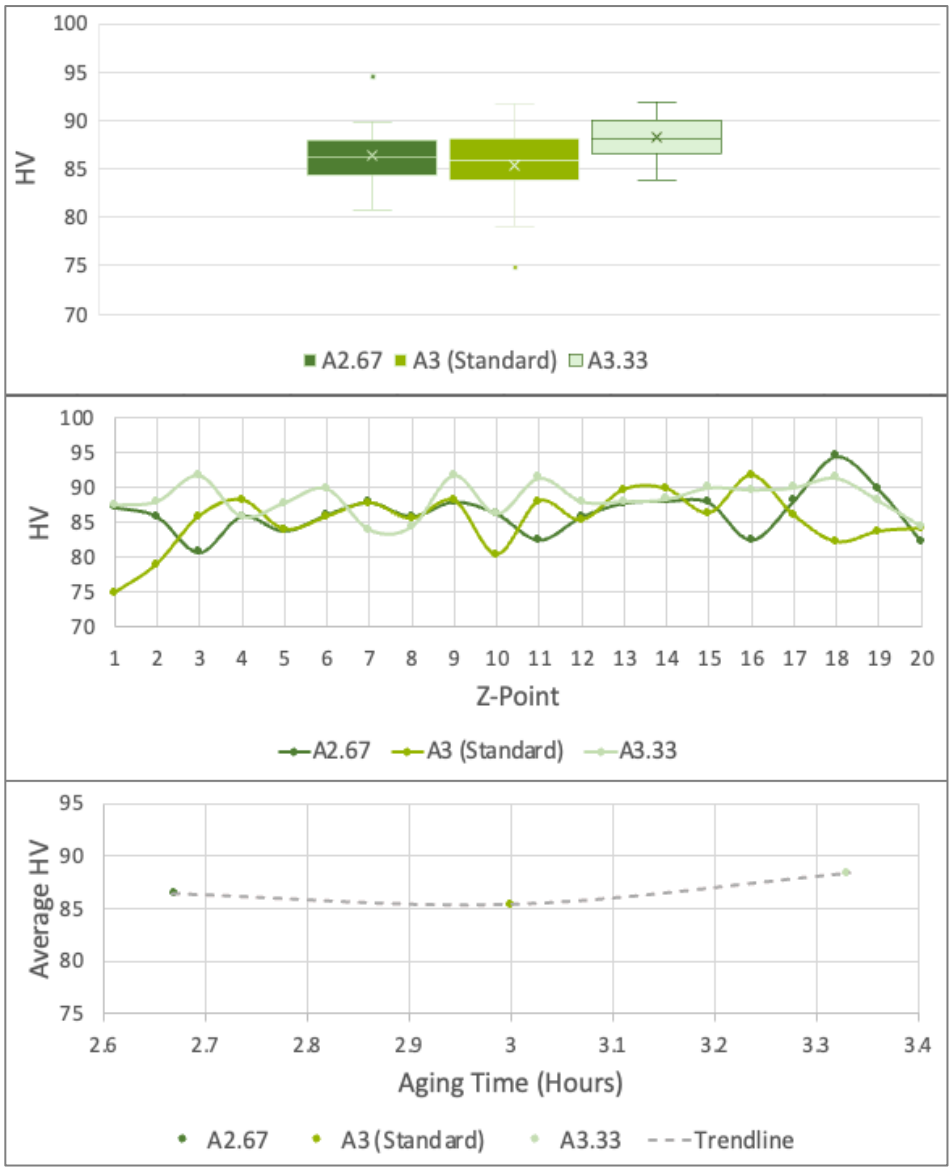

Figure 42. Quantitative HV Results for Varying Aging Time

b. Optical Microscopy

OM images at 100x magnification show very little, if any, variation in changes in particle size. It is not possible to capture Mg_2Si particles in the Al-matrix using OM due to

its magnification limitations. Fine rod-like particles are present in all the samples. These particles are not the Mg_2Si particles that increased strength after age hardening is attributed to but instead are AlFeSi particles. Figure 43 shows all samples from the experiment. Samples with increasing aging time are shown left to right while samples with increasing temperature are show bottom to top.

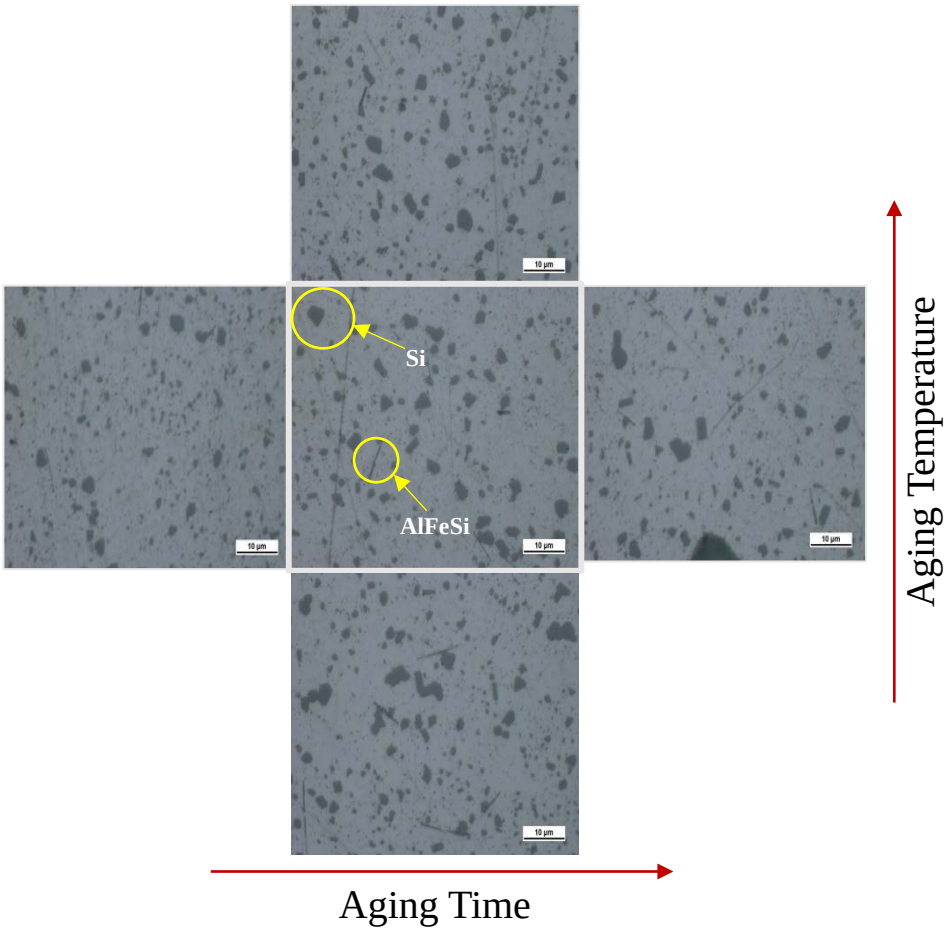

Figure 43. OM Images at 100x Magnification of Samples with increasing Aging Time and Temperature

c. Scanning Electron Microscopy and ImageJ

SEM is used for both varying aging time and temperature analysis of Mg_2Si identification and analysis of particle size.

(3) Aging Temperature Variation

Figure 44 trough Figure 46 shows SEM images at 1,000x and 10,000x magnification at varying aging temperatures with constant aging time of 3 hours. 1,000x magnification captures the Si particles as well as AlFeSi particles. The Si particle show up as darker particles while the rod-like particles have less contrast with the Al-matrix. The 10,000x magnification captures the Mg_2Si particles in the Al-matrix. The Mg_2Si particles are brighter in contrast to the Al-matrix.

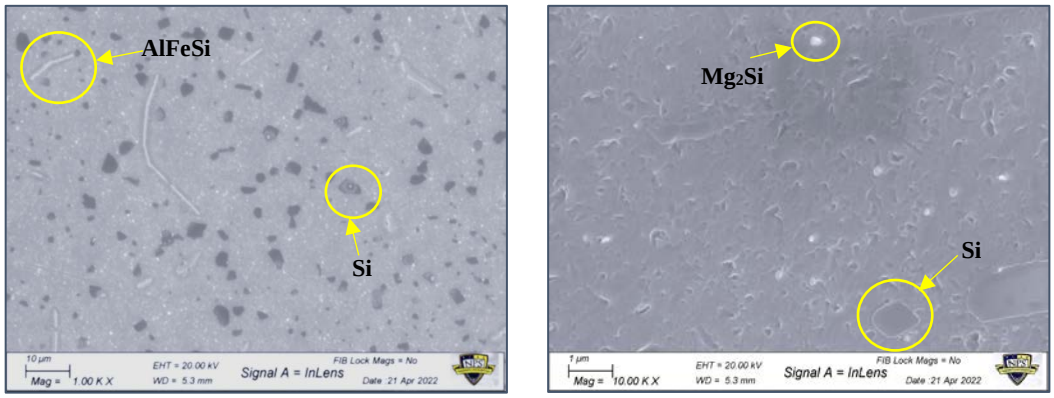

Figure 44. 1,000x (left) and 10,000x Magnification (right) SEM Images for Sample Aged at 140 ºC

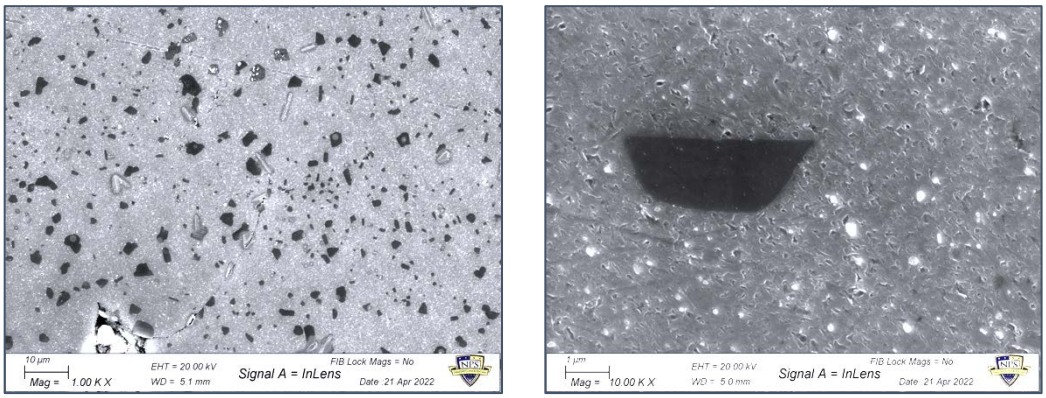

Figure 45. 1,000x (left) and 10,000x Magnification (right) SEM Images for Sample Aged at 155 ºC (Standard Temperature)

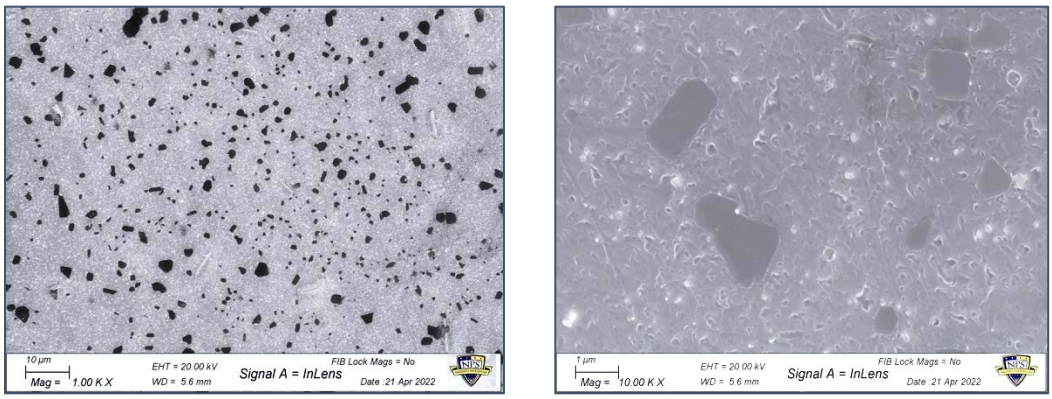

Figure 46. 1,000x (left) and 10,000x Magnification (right) SEM Images for Sample Aged at 170 ºC

The results were very similar to the findings by Xerox. Xerox reported finding needle-like AlFeSi precipitates and “roughly equiaxed [silicon] particles” [9]. Figure 47shows the reported findings by Xerox.

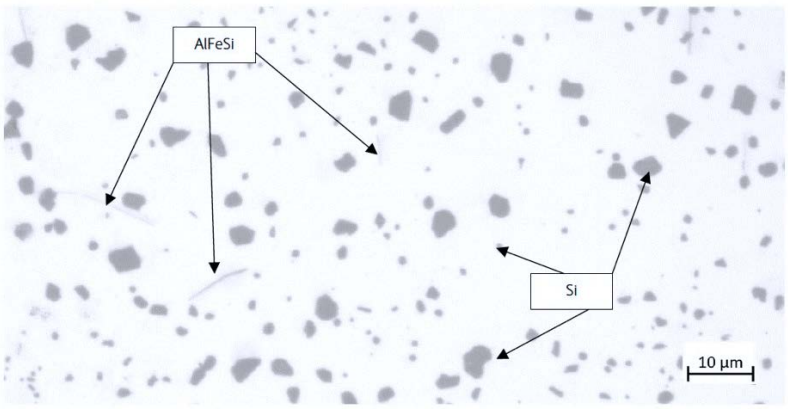

Figure 47. Xerox Reported Microstructure Findings. Source: [9]

Kim et al. [44] studied the effects of heat treatment procedures on the mechanical properties of centrifugally cast A356 alloys and successfully captured Mg_2Si precipitates using field-emission SEM during their study. The study confirmed the heat treatment that resulted in the best mechanical properties for the cast alloy was a T6 heat treatment: solution treatment with quenching in water followed by artificial aging. Figure 48 shows Si, AlFeSi, and Mg_2Si particles in the Al-matrix. The sizes and shapes of the particles are

in line with other findings as well as with the experimental findings presented in this thesis work.

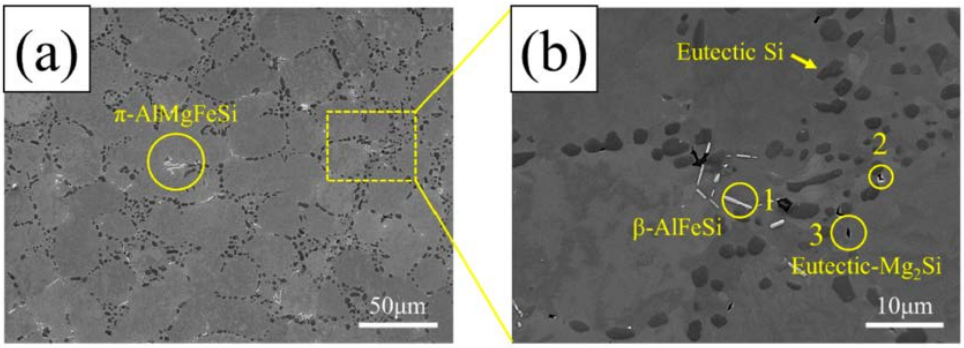

Figure 48. Field-emission Scanning Electron Microscopy of A356 After Heat Treatment. Source: [44]

An EDS point analysis was conducted on what was believed to be Mg_2Si particles. Figure 49 shows the EDS spot analysis of the brighter particle seen in the previous SEM images. The point analysis indicated the presence of 1.25 wt% Mg, 3.34 wt% Si, and 95.40 wt% of Al. It is worth noting that the information from the EDS analysis is semi-quantitative due to lack of a standard sample to compare with.

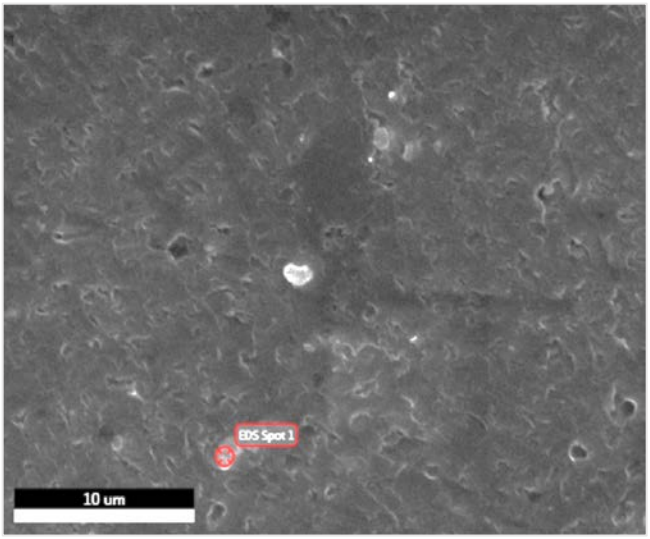

Figure 49. EDS Point Analysis of Mg_2Si Particle

Si and Mg_2Si particle size distribution was compared for samples with varying aging temperatures. Figure 50 shows the plotted Si and Mg_2Si particle size distributions for these samples. Table 7 and Table 8 shows the quantitative analysis of the size distribution reporting the mean, median and mode for each sample. The findings show that aging temperatures at a range of ±15 ºC from the standard temperature of 155ºC does not cause substantial (no more than 3%) differences concerning Mg_2Si particle growth. However, the average Si particle sizes decreased by 15.44%. A possible explanation is that as the aging temperature increases, more Mg_2Si precipitates form, at the expense of Si particles.

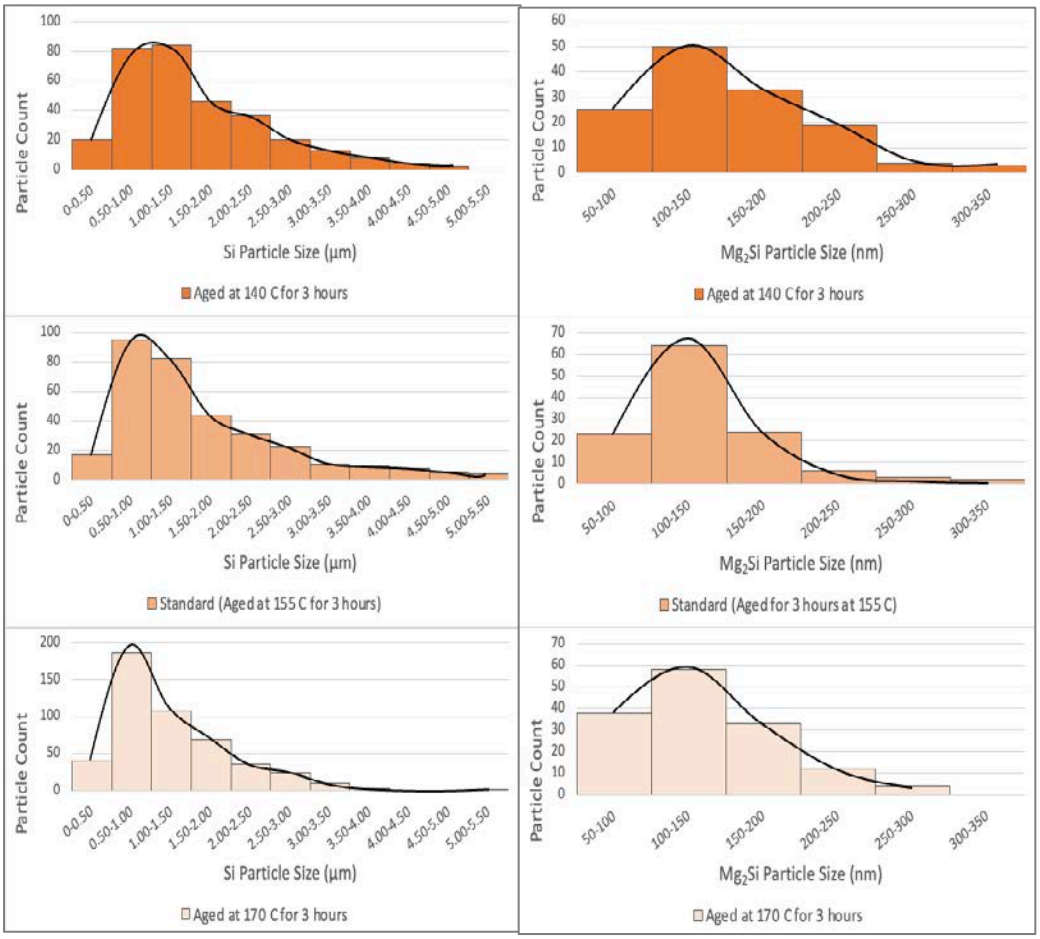

Figure 50. Si and Mg_2Si Particle Size Distribution Box Plots at Varied Aging Temperatures

Table 7. Quantitative Characteristics of Si precipitates for varying aging temperatures

Sample Code	*Aging temperature (℃)*	*Si mean length (μm)*	*Si median length (μm)*	*Si mode length (μm)*
A140	140	1.55	1.30	1.00
A155	155	1.65	1.33	0.89
A170	170	1.26	1.07	0.51

A = Aging. Ex. A140 = Aged at 140 ℃ for 3 hours. Aging temperature is unchanged for all samples reported in this table.

Table 8. Quantitative Characteristics of Mg_2Si precipitates for varying aging temperatures

Sample Code	*Aging temperature (℃)*	*Mg_2Si mean length (nm)*	*Mg_2Si median length (nm)*	*Mg_2Si mode length (nm)*
A140	140	138.29	119.50	108.00
A155	155	141.84	132.00	145.00
A170	170	136.12	131.00	108.00

A = Aging. Ex. A140 = Aged at 140 ℃ for 3 hours. Aging temperature is unchanged for all samples reported in this table.

(4) Aging Time Variation

Figure 51 and Figure 52 shows SEM images of each sample at 1,000x and 10,000x magnification for the samples with varying aging times. These figures are compared to Figure 45 that were aged at the standard temperature and time. The presence of Mg_2Si particles, and the rod-like AlFeSi particles, and Si particles are seen in the images for all samples.

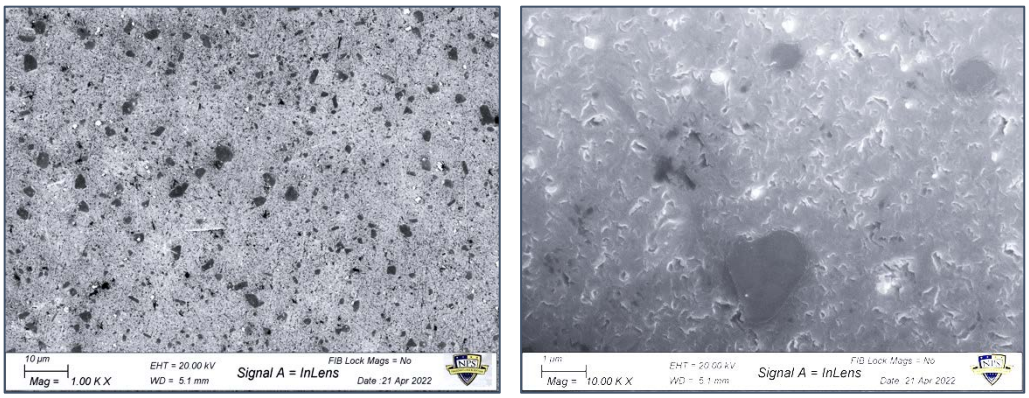

Figure 51. 1,000x and 10,000x Magnification SEM Images of Sample Aged for 2 hours 40 minutes

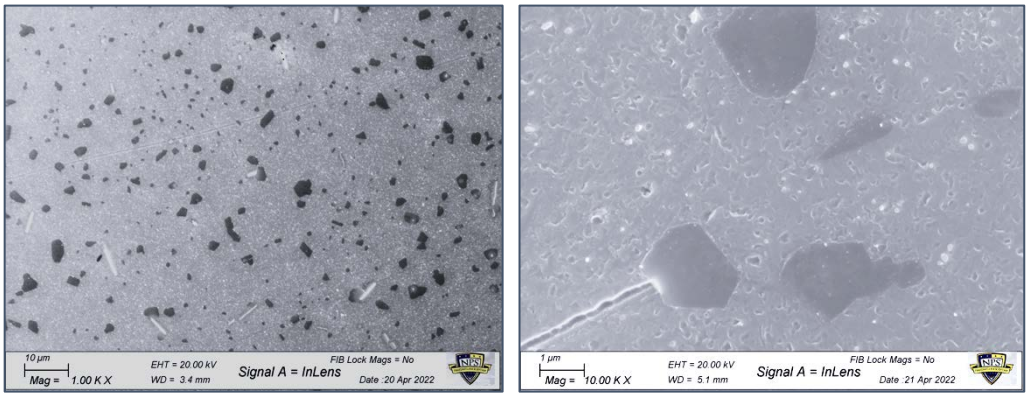

Figure 52. 1,000x and 10,000x Magnification SEM Images of Sample Aged for 3 hours 20 minutes

Figure 53 shows the particle size distribution of all the samples with varying time and constant temperature. Table 9 and Table 10 show quantitative characteristics of the Si and Mg_2Si particle size distribution for all samples reporting the mean, median, and mode. A range of ±20-minute variation from the standard aging time of 3 hours showed an increase of 28.57% for the average Si particle size from time of 2 hours 40 minutes to 3 hours 20 minutes. Conversely, an apparent 35.92% decrease in the average Mg_2Si particle size was measured. Analysis of Figure 51 and Figure 52 also show that a larger number of Mg_2Si precipitates nucleate as the aging time increases. This provides evidence that rather than a particle size reduction with increased aging time, the formation of new Mg_2Si

precipitates is occurring. The data is consistent with the evolution of phases described in Chapter I Section D.2 concerning G-P zones.

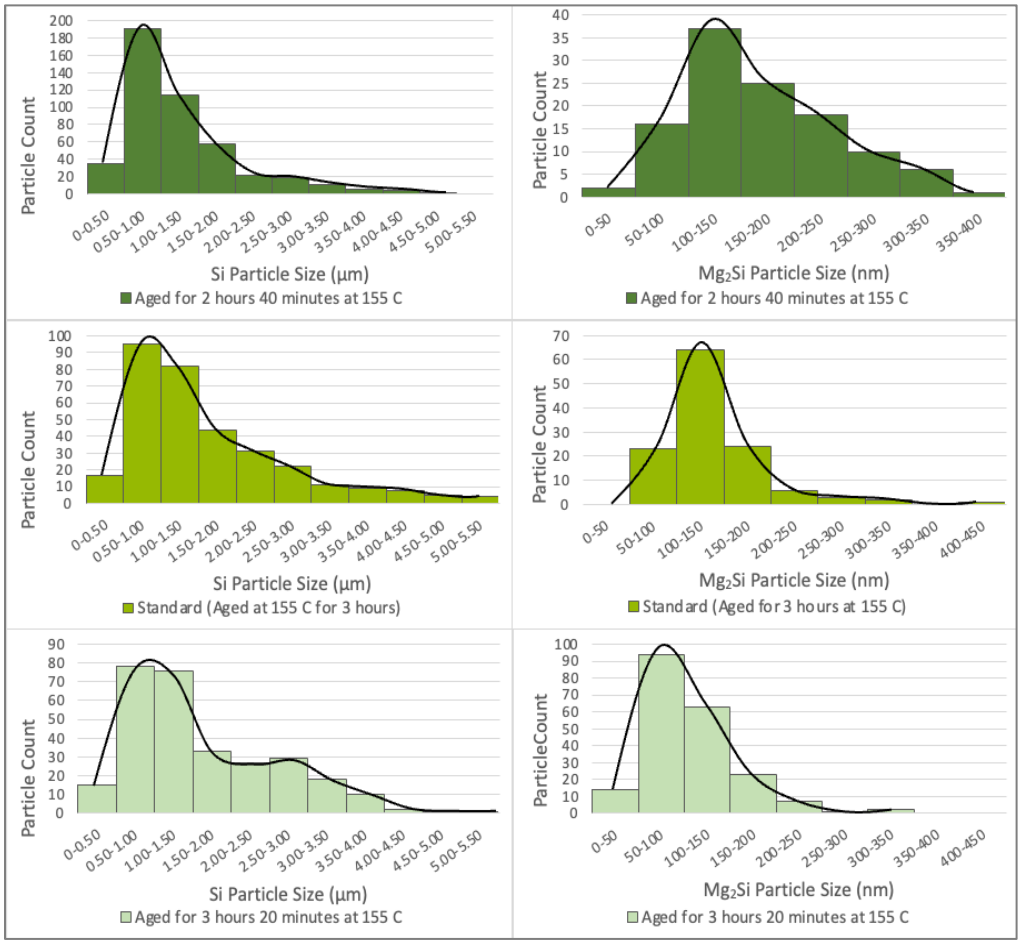

Figure 53. Mg_2Si Particle Size Distribution at Varying Aging Times

Table 9. Quantitative Characteristics of Si precipitates for varying aging times

Sample Code	*Aging time (hours)*	*Si mean length (µm)*	*Si median length (µm)*	*Si mode length (µm)*
A2.67	2.67	1.26	1.01	1.00
A3	3.00	1.65	1.33	0.890
A3.33	3.33	1.62	1.302	0.567

A = Aging. Ex. A2.67 = Aged for 2.67 hours at 155 ℃. Aging temperature is unchanged for all samples.

Table 10. Quantitative Characteristics of Mg_2Si precipitates for varying aging times

Sample Code	*Aging time (hours)*	*Mg_2Si mean length (nm)*	*Mg_2Si median length (nm)*	*Mg_2Si mode length (nm)*
A2.67	2.67	167.91	156.5	143.00
A3	3.00	141.84	132.00	145.00
A3.33	3.33	107.59	98.00	78.00

A = Aging. Ex. A2.67 = Aged for 2.67 hours at 155 ℃. Aging temperature is unchanged for all samples.

B. AS-PRINTING ARGON ADDITION ENVIRONMENT EFFECTS

Inert gas in the AM environment is essential to minimize the effects of reactive gases found in the air. This experiment tested the effects of additional argon in the ElemX 3D printing environment. The aim of adding argon to the environment was to avoid delamination and lack of inter-layer adhesion due to oxidation. Improvements would also result in improved strength of the material. As described in the experimental methods, an argon injector was designed, printed, and integrated into the existing 3D printer, see Chapter II Sections B.1,2, and 3. The outcomes of 3D printing blocks from which tensile specimens were machined and tested with and without the extra argon in the environment are presented in the sections below.

1. Tensile Test Results

The tensile specimens were tested, and their yield strength (YS) and ultimate tensile strength (UTS) values were compared. Figure 54 and Figure 55 show the YS and UTS spread for both standard and added argon environment and their respective printing orientation. The results were compared to the results of other identical 3D prints fabricated in a standard printing environment that were printed horizontally and vertically. All samples were compared to the reported Xerox YS and UTS for XY orientation prints of 179 and 289 MPa, respectively [24]. The strength values for a vertical print orientation, or Z-direction, is typically less than a horizontal print orientation, or XY-direction. The specimens produced with added argon showed lower strength results than a vertically printed part at an average 138.23 MPa for yield strength and 262.35 MPa for ultimate

tensile strength. In comparison, the experimental standard resulted in an average of 154.39 MPa for yield strength and 275.37 MPa for ultimate tensile strength. A decrease of 10.47% in YS and 4.73% in UTS.

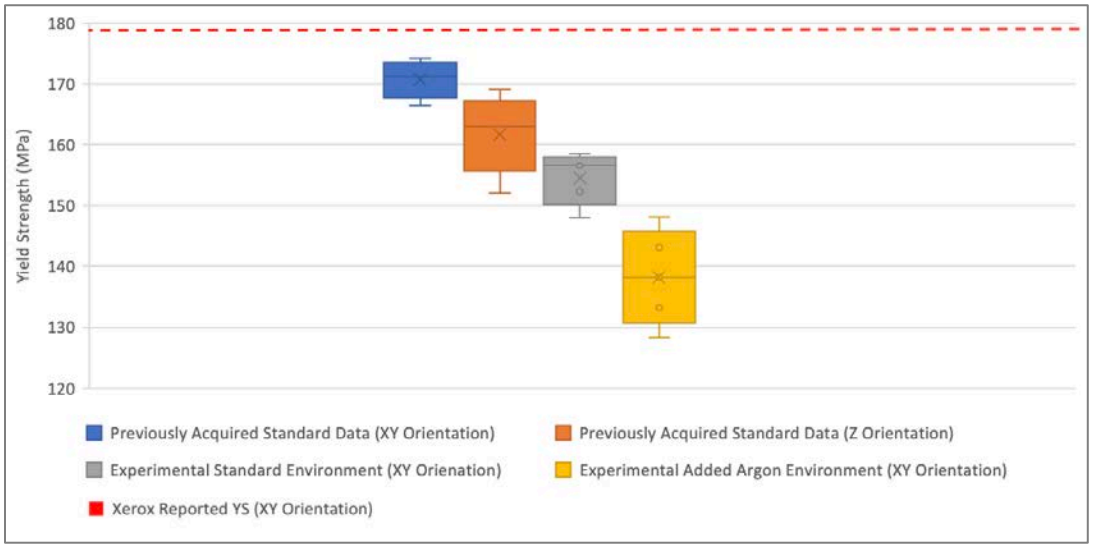

Figure 54. Yield Strength (YS) Box-and-whisker plot of samples

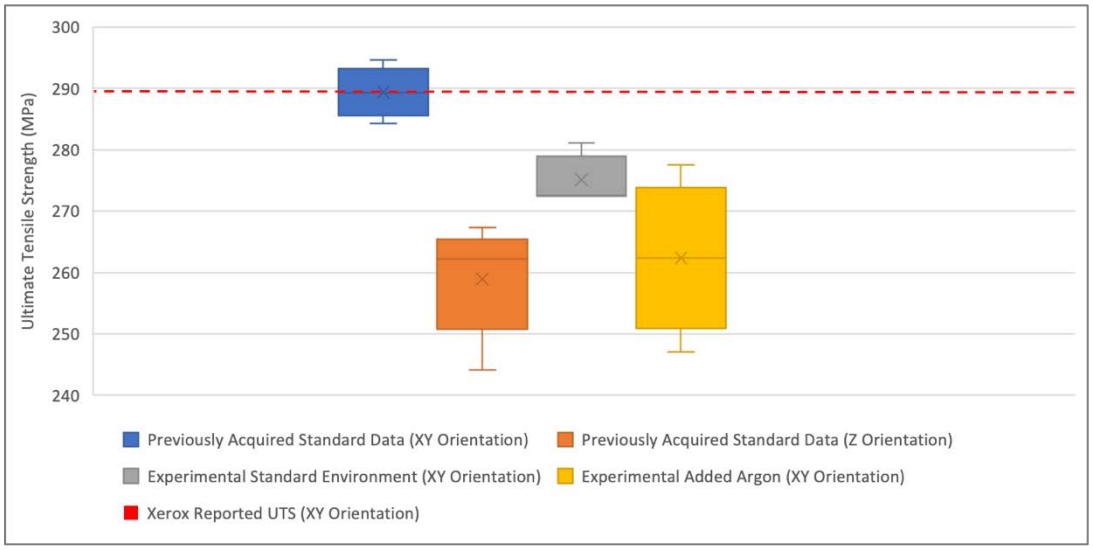

Figure 55. Ultimate Tensile Strength (UTS) Box-and-whisker plots of samples

A hypothesis of the results is that the argon from the injector was negatively affecting the jet stream resulting in a higher level of porosity causing detrimental outcomes for the mechanical properties. It is believed that a parametric study to identify the optimized conditions for introduction of the argon stream has potential benefits and could be explored in future studies. The analysis of the microstructure supports this statement and is presented in the following sections.

2. Optical Microscopy Results

Figure 56 shows OM images at 2.5x magnification of the standard and added argon environment prints taken from a cross-section of the specimens avoiding the necking area. The size and number of pores observed in both samples are similar.

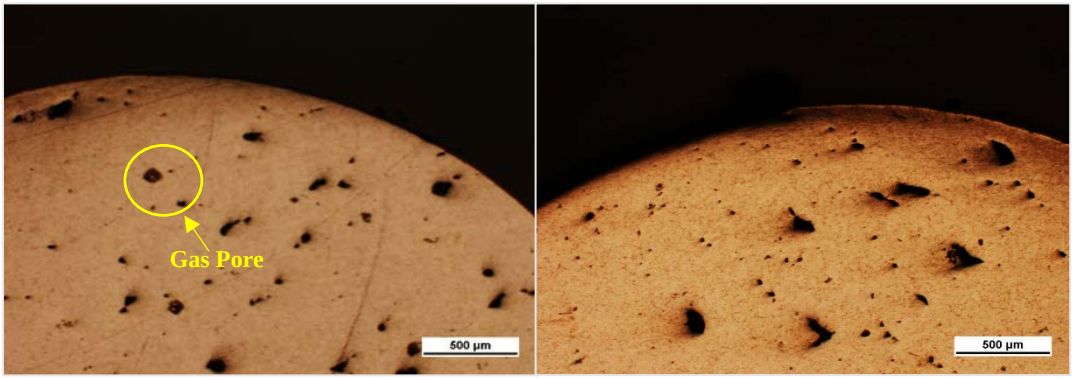

Figure 56. OM Images at 2.5x magnification of Standard (left) vs Added Argon (right) Environment Sample Surfaces.

3. Scanning Electron Microscopy/Energy-Dispersive X-Ray Results

Figure 57 through Figure 58 shows SEM images of the sections where the tensile specimens separated during tensile testing for the standard and added argon environments at 100x, 500x, and 1,000x magnification. The porosity throughout the surface is pronounced along with the delamination in between the layers. Delamination occurs in the same direction throughout the samples surface indicating that it is occurring in between the printing layers caused by oxidation. Contaminants can be seen at 100x and 500x magnification in both samples.

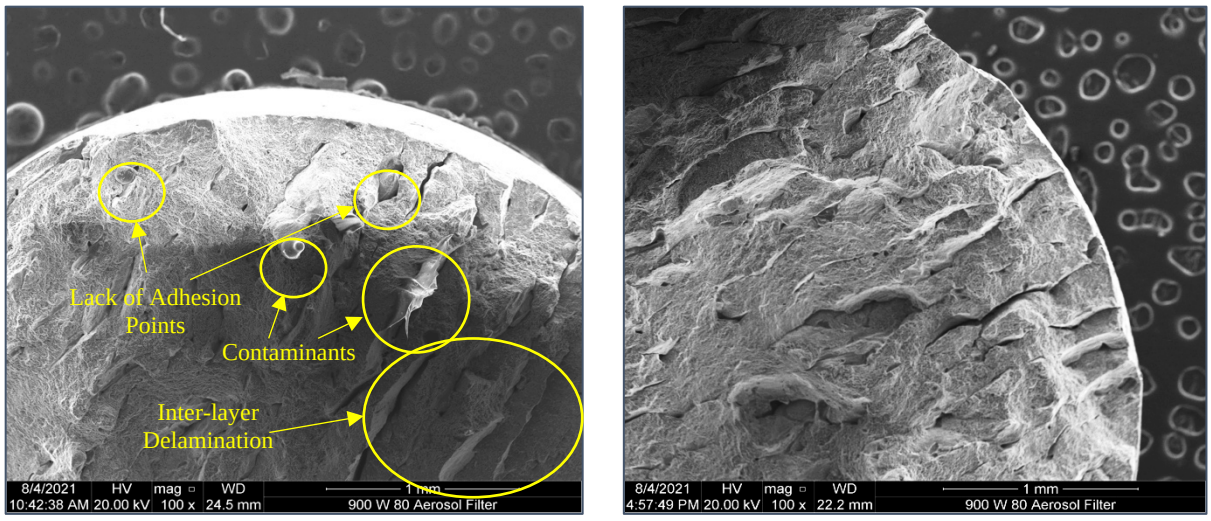

Figure 57. 100x Magnification SEM Images of Failed Surfaces for Standard (left) vs Added Argon Environment (right)

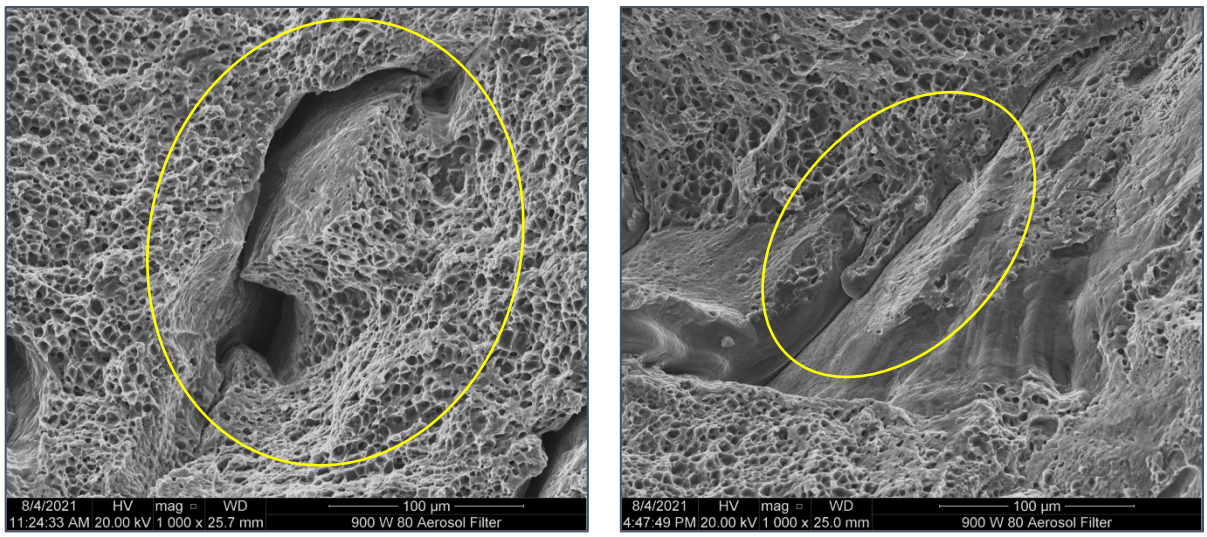

Figure 58. 1,000x Magnification SEM Images of Failed Surfaces for Standard (left) vs Added Argon Environment (right) with Lack of Fusion and Delamination

Figure 59 shows the results from an EDS point analysis conducted on a contaminant found on a sample printed in a standard environment. The results show presence of carbon at the contaminant sighting indicating a dust particle found embedded in the 3D prints.

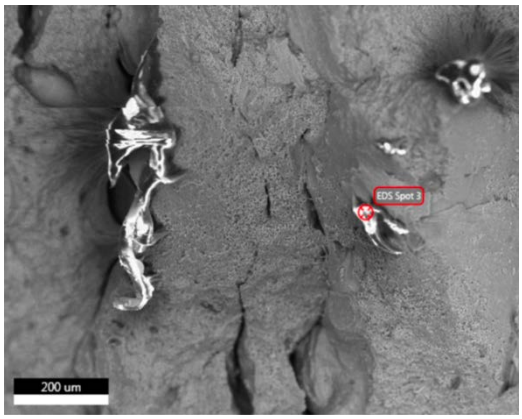

Figure 59. EDS Point Analysis of Contaminant in Experimental Standard Environment Print

An EDS point analysis was also conducted at a typical spot for comparison and is shown in Figure 60. The results of the EDS point analysis shown in Figure 42 indicate 83.47 wt% aluminum and 16.53 wt% silicon and is typical for the A356/Al 4008 alloy.

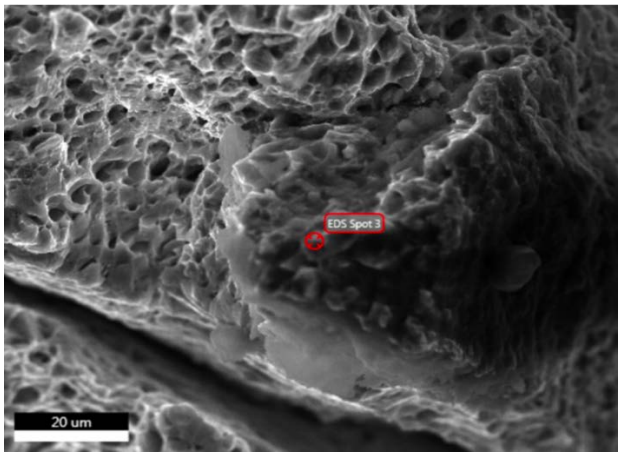

Figure 60. EDS Point Analysis of Previously Acquired Standard Data (Horizontal Print)

In summary, 3 experiments were conducted to evaluate the process from printing to post-printing processes of a 3D part fabricated using the ElemX liquid metal printer. The results show that the 3D part achieves its highest hardness when it is quenched within the first minute upon completion of print. The Solution treatment at the time and temperature

used can only reverse the detrimental effects caused by quenching delays to a certain threshold. The hardness of the 3D part is dependent on the presence of Si and the nucleation and growth of Mg_2Si. The growth of Si particles during solution treatment highly influences the 3D parts increase in hardness. Aging helps bring precipitates out of solution resulting in increased hardness with increased time or temperature for this process. The increase in aging temperature or time, though, does not necessarily result in larger Si or Mg_2Si particles but instead the presence of more particles in the solution. No overaging was observed in any of the conditions employed.

IV. CONCLUSION AND FUTURE STUDIES

The objective with these studies was to verify the optimal conditions to be employed in the post-printing processes of additively manufactured (AM) aluminum 4008 parts via liquid metal jetting.

These studies have proven that the T6 heat treatment is essential and ensures the optimal mechanical properties of additively manufactured parts. The use of these processes intended for A356 cast alloys is also applicable to liquid metal jetted (LMJ) AM parts.

The results from the quenching experiment showed that hardness of the 3D parts after solution treatment increased by 36.42%, from an average 59.64 HV to 81.36 HV. Not only does solution treatment improve the hardness of the 3D part but it can also reverse damaging effects that were initiated by a delay to quenching after 3D fabrication. The sample that was quenched immediately after the completion of printing (sample S0) had the highest hardness average at 86.79 HV which is an increase of 6.67% from the overall average of the solution treated samples. This indicates that the critical time between print completion and quenching is within the first minute, longer delays cause effects at the microstructural level that decease the hardness of the 3D part. The effects from a delay to quenching could not be corrected with the prescribed solution treatment time and temperature. Prior to solution treatment, the Q4 sample reported the lowest hardness but after solution treatment the S4 sample reported an increase in hardness with it being on trend with the other samples that also experienced delays to quenching (Q1-Q5).

The experiment conducted on varying aging times and temperatures further proved that the heat treatment procedures established for A356 cast alloy are also pertinent to AM applications. An increase in aging temperature with constant time showed a gradual 1.87% increase in hardness and increasing aging time with constant temperature showed a 2.28% increase.

A range of ± 15 ºC or ± 20 minutes variation from the standard aging temperature of 155 ºC and time of 3 hours showed an increase of 28.57% for the average Si particle size from time of 2 hours 40 minutes to 3 hours 20 minutes. Conversely, an apparent

35.92% decrease in the average Mg_2Si particle size was measured. Analysis of the microstructure showed that a larger number of Mg_2Si precipitates nucleate as the aging time increases. This provides evidence that rather than a particle size reduction with increased aging time, the formation of new Mg_2Si precipitates is occurring. The data is consistent with the evolution of phases described previously in this thesis and by other works. The observations made in this study correspond to solution treatment times and temperatures specified in well studied cast alloy standards; modifications to those variables render different outcomes.

Air in the printing environment is a well-known issue in AM. Inert gas is used to combat their effects. The specimens produced with added argon showed lower strength results than a vertically printed part at an average 138.23 MPa for yield strength and 262.35 MPa for ultimate tensile strength. In comparison, the experimental standard resulted in an average of 154.39 MPa for yield strength and 275.37 MPa for ultimate tensile strength. A decrease of 10.47% in YS and 4.73% in UTS. It is believed that the argon from the injector was negatively affecting the jet stream resulting in a higher level of porosity causing detrimental outcomes for the mechanical properties. A parametric study to identify the optimized conditions for introduction of the argon stream has potential benefits and could be explored in future studies.

Overall, the experiments conducted successfully showed how quenching, solution treatment, and aging have an impact on the print's mechanical properties and microstructure. As for inert gases, further studies into better argon addition applications can further improve the quality of the 3D prints made via LMJ. This study formed a deeper understanding of the variables that influence the mechanical properties and what will enable achievement of higher quality 3D parts.

APPENDIX. VICKERS HARDNESS IN XY-DIRECTION RESULTS

Similar observations to those presented in Chapter III for the quenched specimens in the Z-direction were also observed for the measurements performed in the XY-direction, as shown in Figures 61 and 62.

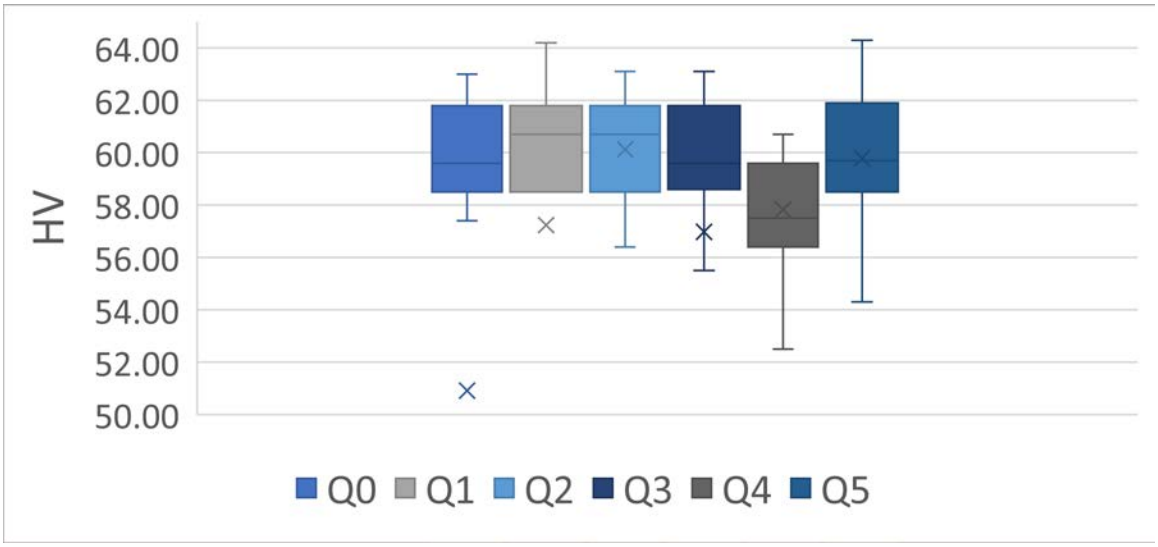

Figure 61. As Quenched Vickers Hardness Test Results in XY-Direction

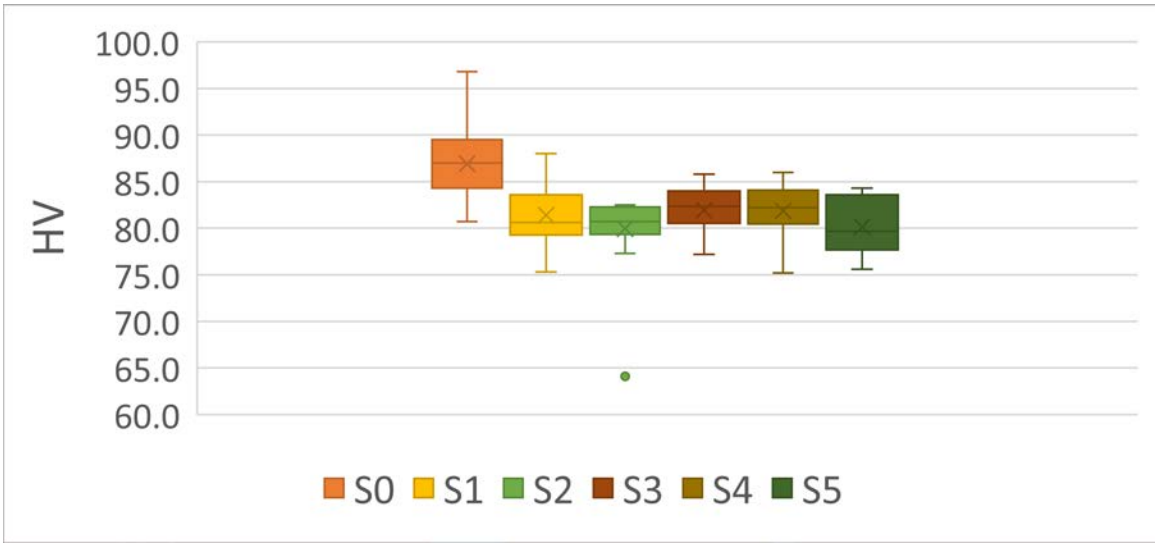

Figure 62. After Solution Treatment Vickers Hardness Test Results in XY-Direction

THIS PAGE INTENTIONALLY LEFT BLANK

LIST OF REFERENCES

[1] Joint Defense Manufacturing Council, Office of the Deputy Director for Strategic Technology Protection and Exploitation, and Office of the Under Secrectary of Defense for Reasearch and Engineering, "Department of Defense Additive Manufacturing Strategy," Washington, D.C., Strategy DOPSR case #21-S-0711 applies, Jan. 2021. [Online]. Available: https://www.cto.mil/wp-content/uploads/2021/01/dod-additive-manufacturing-strategy.pdf

[2] ISO, "Additive Manufacturing-General principles-Terminology." 2018. [Online]. Available: https://www.iso.org/obp/ui/#iso:std:iso-astm:52900:dis:ed-2:v1:en

[3] Hybrid Manufacturing Technologies, "7 Families of Additive Manufacturing." [Online]. Available: https://www.additivemanufacturing.media/cdn/cms/7_families_print_version.pdf

[4] C. V., *3Dnatives*, "What are the risks associated with FDM and metal 3D printing?," May 2020, [Online]. Available: https://www.3dnatives.com/en/risks-associated-with-fdm-metal-3d-printing-190520205/

[5] Xerox, "Xerox ElemX Liquid Metal 3D Printer System Specifications." 2021. [Online]. Available: https://www.xerox.com/downloads/usa/en/3d-printing/xerox-elemx-3dprinter-system-specifications-ENUS.pdf

[6] H. B. Martin, "Xerox's first 3D printer lands at a California Navy college," *Addit. Rep.*, Aug. 2021, [Online]. Available: https://www.thefabricator.com/additivereport/article/additive/xeroxs-first-3d-printer-lands-at-a-california-navy-college

[7] A. Elliott, A. Shyam, O. Rios, and T. Muth, *OAK RIDGE Natl. Lab.*, "Advancing Liquid Metal Jet Printing," Sep. 2019, [Online]. Available: http://www.osti.gov/scitech/

[8] S. Farooqi, *engineering.com*, "One Drop at a Time: Xerox 3D Prints with Liquid Metal,," Feb. 2021. [Online]. Available: https://www.engineering.com/story/one-drop-at-a-time-xerox-3d-prints-with-liquid-metal

[9] C. Fletcher, Xerox, "Metallography Guide For Xerox 4008 Aluminum Wire." [Online]. Available: https://www.xerox.com/downloads/usa/en/3d-printing/ElemX-Metallography-Guide.pdf

[10] ASM International, *ASM handbook. 2: Properties and selection: nonferrous alloys and special-purpose materials*, 7. print. Materials Park, Ohio: ASM International, 2007.

[11] J. R. Davis & Associates and ASM International, Eds., *Aluminum and aluminum alloys*. Materials Park, OH: ASM International, 1993.

[12] S. Lathabai, "Additive Manufacturing of Aluminium-Based Alloys and Composites," in *Fundamentals of Aluminium Metallurgy*, Elsevier, 2018, pp. 47–92. doi: 10.1016/B978-0-08-102063-0.00002-3.

[13] Total Materia, "AlMgSi Alloys," *Total Mater.*, Oct. 2014, [Online]. Available: https://www.totalmateria.com/page.aspx?ID=CheckArticle&LN=EN&site=ktn&NM=348

[14] United States Welding Corporation. "4008 (A356)." [Online]. Available: https://www.usweldingcorp.net/TDS/tds4181.pdf

[15] Milwaukee Precision Casting Inc. "A356 Aluminum Castings & Treatments." [Online]. Available: https://www.milwaukeeprec.com/a356.html

[16] "Mechanical properties of as-built A356 aluminium alloy processed by Selective Laser Melting," *Met. Addit. Manuf.*, Jan. 2015, [Online]. Available: https://www.insidemetaladditivemanufacturing.com/blog/-mechanical-properties-of-as-built-a356-aluminium-alloy-processed-by-selective-laser-melting

[17] Total Materia, "Heat Treatable Aluminum Alloys," *Total Mater.*, Apr. 2002, [Online]. Available: https://www.totalmateria.com/Article39.htm

[18] The Editors of Encyclopaedia Britannica, "quenching," *Encyclopaedia Britannica*. [Online]. Available: https://www.britannica.com/technology/quenching-materials-processing

[19] S. Seifeddine, Giulio Timelli, and Ingvar L. Svensson, "Influence of quenching rate on the microstructural and mechanical properties of aluminum cast alloys A356 and A354," *Int. Foundry Res.*, pp. 2–10, 2007.

[20] L&L Special Furnace Co, Inc., "Types of Aluminum Heat Treatments." Nov. 02, 2018. [Online]. Available: https://llfurnace.com/blog/types-of-aluminum-heat-treatments/

[21] E. Sjölander and S. Seifeddine, "Artificial ageing of Al–Si–Cu–Mg casting alloys," *Mater. Sci. Eng. A*, vol. 528, no. 24, pp. 7402–7409, Sep. 2011, doi: 10.1016/j.msea.2011.06.036.

[22] M. Rahman, S. H. Sabbir, M. S. Kabir, M. S. Kaiser, and M. A. Nur, "Study of precipitation behaviour of hyper-eutectic Al-Si automotive alloy," Surabaya, Indonesia, 2018, p. 030013. doi: 10.1063/1.5044292.

[23] W. D. Callister and D. G. Rethwisch, *Materials science and engineering: an introduction*, 9th edition. Hoboken, NJ: Wiley, 2014.

[24] Xerox, “Xerox ElemX 3D Printer Material Data Sheet.,” Dec. 2021. [Online]. Available: https://www.xerox.com/downloads/usa/en/3d-printing/xerox-elemx-3dprinter-material-safety-data-sheet-ENUS.pdf

[25] L. J. Colley, “Microstructure-Property Models For Heat Treatment of A356 Aluminum Alloy,” *Univ. Br. Columbia*, Mar. 2011, [Online]. Available: https://central.bac-lac.gc.ca/.item?id=TC-BVAU-33142&op=pdf&app=Library&oclc_number=1032912412

[26] L. Wu and W. G. Ferguson, “Modelling of Precipitation Hardening in Casting Aluminium Alloys,” *Mater. Sci. Forum*, vol. 618–619, pp. 203–206, Apr. 2009, doi: 10.4028/www.scientific.net/MSF.618-619.203.

[27] Primary Foundry Alloys, “Technical Data Sheet AlSi7Mg0.3.” [Online]. Available: http://cdn.thomasnet.com/ccp/00176659/102129.pdf.

[28] A. Morri, “Correlations among microstructure, effect of thermal exposure and mechanical properties, in heat treated Al-Si-Mg and Al-Cu aluminum alloys,” *Univ. Politec. Delle Marche*, Jan. 2012.

[29] S. J. Andersen, C. D. Marioara, J. Friis, S. Wenner, and R. Holmestad, “Precipitates in aluminium alloys,” *Adv. Phys. X*, vol. 3, no. 1, p. 1479984, Jan. 2018, doi: 10.1080/23746149.2018.1479984.

[30] G. Guo, Q. Wang, Y. Rong, and R. D. Sisson, “Modeling the Yield Strength of an A356 Aluminum Alloy during the Aging Process,” *Mater. Perform. Charact.*, vol. 9, no. 1, p. 20200081, Jan. 2020, doi: 10.1520/MPC20200081.

[31] P. Forêt, “Inert Gas in Metal 3D Printing, Materials, and Postprocessing,” *Addit. Manuf.*, Mar. 2019.

[32] M. Walter and D. Bauer, “The Influence of Process Gas on Additively Manufactured AlSi10Mg [White paper],” EOS GmbH, Munich, Germany, White paper. [Online]. Available: https://www.linde-gas.com/en/images/EOS_Whitepaper_Linde_en_WEB_tcm17-641228.pdf

[33] I. V. Shishkovsky, Ed., *New Trends in 3D Printing*. InTech, 2016. doi: 10.5772/61398.

[34] M. P., “What is a G-code and What is its Use in 3D Printing?,” *3Dnatives*, Sep. 2021, [Online]. Available: https://www.3dnatives.com/en/g-code-use-3d-printing-230920216/#!

[35] P. Basiliere, “First Look: ElemX 3D Metal Printer,” Apr. 28, 2021. https://monadnockinsights.com/2021/04/28/first-look-elemx-3d-metal-printer/

[36] The Editors of Encyclopaedia Britannica, “Vickers hardness.” Dec. 06, 2018. [Online]. Available: https://www.britannica.com/science/Vickers-hardness

[37] EMCO-TEST, “How is a Vickers hardness value read and represented?” [Online]. Available: https://www.emcotest.com/en/the-world-of-hardness-testing/hardness-know-how/theory-of-hardness-testing/vickers/how-is-a-vickers-hardness-value-read-and-represented/

[38] Research Services Branch, *ImageJ*. [Online]. Available: https://imagej.nih.gov

[39] Xerox, “Xerox ElemX 3D Printer Design Guide V1.0.” Xerox, 11/21. [Online]. Available: https://www.xerox.com/downloads/usa/en/3d-printing/xerox-elemx-3dprinter-design-guide-v1-ENUS.pdf

[40] T. Wang, Y. Zheng, Z. Chen, Y. Zhao, and H. Kang, “Effects of Sr on the microstructure and mechanical properties of in situ TiB2 reinforced A356 composite,” *Mater. Des.*, vol. 64, pp. 185–193, Dec. 2014, doi: 10.1016/j.matdes.2014.07.040.

[41] M. Ibrahim, M. Abdelaziz, A. Samuel, H. Doty, and F. Samuel, “Spheroidization and Coarsening of Eutectic Si Particles in Al-Si-Based Alloys,” *Adv. Mater. Sci. Eng.*, vol. 2021, pp. 1–16, Jan. 2021, doi: 10.1155/2021/6678280.

[42] S. Ma, M. D. Maniruzzaman, D. S. MacKenzie, and R. D. Sisson, “A Methodology to Predict the Effects of Quench Rates on Mechanical Properties of Cast Aluminum Alloys,” *Metall. Mater. Trans. B*, vol. 38, no. 4, pp. 583–589, Aug. 2007, doi: 10.1007/s11663-007-9044-3.

[43] X. Zhu, H. Yang, X. Dong, and S. Ji, “The effects of varying Mg and Si levels on the microstructural inhomogeneity and eutectic Mg2Si morphology in die-cast Al–Mg–Si alloys,” *J. Mater. Sci.*, vol. 54, no. 7, pp. 5773–5787, Apr. 2019, doi: 10.1007/s10853-018-03198-6.

[44] W. Kim, K. Jang, C. Ji, and E. Lee, “Effects of Heat Treatment on the Microstructure and Hardness of A356 (AlSi7Mg0.3) Manufactured by Vertical Centrifugal Casting,” *Appl. Sci.*, vol. 11, no. 23, p. 11572, Dec. 2021, doi: 10.3390/app112311572.

INITIAL DISTRIBUTION LIST

1. Defense Technical Information Center
   Ft. Belvoir, Virginia

2. Dudley Knox Library
   Naval Postgraduate School
   Monterey, California